Interferometric Processing of TanDEM-X Images for Forest Height Estimation

Daniel Molina Hurtado

Department of Radio Science and Engineering

School of Electrical Engineering

Aalto University

A final project submitted for the degree of

Telecommunications Engineering

Supervised by Jaan Praks

2012 May

Author: Daniel Molina Hurtado

Name of the Thesis: Interferometric Processing of TanDEM-X Images for Forest Height Estimation.

Date: 30.5.2012

Number of Pages: 83

Department: Department of Radio Science and Engineering

Professorship: Space Technology

Supervisor: Mr. Jaan Praks

Abstract:

Biomass is one of the most desired parameters for applications like climate modelling, resource assessment or wood industry. By using allometry equations (82) it is possible to obtain biomass information from canopy height. Some studies have demonstrated that current interferometric techniques applied to airborne Synthetic Aperture Radar (SAR) images can provide fairly accurate estimates of tree height (45, 52, 53, 54). Space based interferometric methods can provide global estimates of canopy height but they require very accurate orbit information. In this work the ability of the recently launched SAR satellites TerraSAR-X and TanDEM-X to estimate canopy height is evaluated.

To do this, a complete interferometric processing chain is created including SAR data reading into memory, complex interferogram calculation, interferogram flattening by flat Earth approximation and image transformation to geographical coordinates. Finally the resulting phase height maps are compared with a digital elevation model and a canopy height model of the terrain under study as well as with X-band E-SAR data from the FINSAR campaign (52, 53, 54) of the same area.

Key Words: Synthetic Aperture Radar, Interferometry, Biomass, Forest, Forest Height, Coherence, Interferogram, Digital Elevation Model, Canopy Height Model, TerraSAR-X and TanDEM-X.

To Julia, for her love and support all these years.

Preface

This final project has been carried out in the Department of Radio Science and Engineering of Aalto University between October 2011 and May 2012 under the supervision of Mr. Jaan Praks.

First of all, I would like to thank Mr. Praks for giving me the chance of working in this project and for its attentive supervision during these months.

Secondly, I would like to thank the Polytechnic University of Valencia for making possible my stay in Finland as part of the Erasmus program and also the staff of Aalto University for their kindness and help during my stay.

I am also grateful to all the members of the Department of Radio Science and Engineering for making me feel integrated and comfortable at work at every moment.

I can not forget to thank my fellow student and great friend Joaquín Antón for its inestimable friendship and support during the last three years.

For last I would like to thank especially my parents María del Carmen and José Ángel and my sister Laura for its support and trust during all my study years and also my grandmother Carmen for looking after me since I can remember. Without them, I would not be writing these lines that conclude my telecommunication engineering studies.

May 30, 2012

Daniel Molina Hurtado

Contents

List of Figures

List of Tables

Nomenclature

List of Acronyms

2D Two-dimensional

3D Three-dimensional

CHM Canopy Height Model

COSAR Complex SAR

CoSSC Co-registered Single-look Slant-range Complex

DEM Digital Elevation Model

DLR German Aerospace Center

DSM Digital Surface Model

EM Electromagnetic

FFT Fast Fourier Transform

FM Frequency Modulated

FT Fourier Transform

IFFT Inverse FFT

InSAR SAR Interferometry

JPL Jet Propulsion Laboratory

LIDAR Light Detection And Ranging

NASA National Aeronautics and Space Administration

NOAA National Oceanic and Atmospheric Administration

Pol-InSAR Polarimetric SAR Interferometry

PolSAR SAR Polarimetry

PRF Pulse Repetition Frequency

RCMC Range Cell Migration Correction

RDA	Range/Doppler algorithm
RMS	Root Mean Square
SAR	Synthetic Aperture Radar
TDX	TanDEM-X
TSX	TerraSAR-X
UTM	Universal Transverse Mercator
WGS-84	World Geodetic System 1984 revision

List of Symbols

α	Attenuation constant
α	Baseline tilt angle with respect to the horizontal
β	Depression angle
β	Propagation constant
δ	Penetration depth
ϵ	Absolute complex electric permittivity
ϵ'	Real part of the absolute complex electric permittivity
ϵ''	Imaginary part of the absolute complex electric permittivity
ϵ_0	Electric permittivity of vacuum
ϵ_c	Complex electric permittivity
ϵ_r	Relative complex electric permittivity
ϵ'_r	Real part of the relative complex electric permittivity
ϵ''_r	Imaginary part of the relative complex electric permittivity
γ	Complex interferometric Coherence
$\hat{u}_h$	Unit vector representing the direction of the horizontally polarized component of an EM wave
$\hat{u}_v$	Unit vector representing the direction of the vertically polarized component of an EM wave
λ	Wavelength
μ	Magnetic permeability
μ_0	Magnetic permeability of vacuum
ω_0	Radian frequency
Φ	Look angle

ϕ	Interferometric phase difference
σ	Conductivity
$\tan(\delta)$	Loss tangent
τ	Length of the transmitted pulse
θ	Incidence angle
θ_0	Incidence angle in the absence of relief for a given range
φ	Interferometric phase
$\vec{E^i}$	Electric field vector of the incident EM wave on a target
$\vec{E^s}$	Electric field vector of the scattered EM wave from a target
$\vec{E_h}$	Electric field vector of the horizontally polarized component of an EM wave
$\vec{E_v}$	Electric field vector of the vertically polarized component of an EM wave
$\vec{E}$	Electric field vector
$\vec{H}$	Magnetic field vector
$\vec{r}$	Distance vector
B	Physical interferometric baseline length
B_D	Doppler bandwidth
B_n	Perpendicular baseline
c	Wave propagation speed in the medium
c_0	Speed of light
E^i	Electric field amplitude of the incident EM wave from a target
E^s	Electric field amplitude of the scattered EM wave from a target
E_0	Electric field amplitude
E_h	Electric field amplitude of the horizontally polarized component of an EM wave
E_v	Electric field amplitude of the vertically polarized component of an EM wave
f	Frequency
f_0	Center frequency of the radar signal
f_D	Doppler frequency shift
G_R	Ground-range distance from the radar to a target
G_r	Ground range distance between 2 targets
H	SAR platform altitude
k	Wavenumber

k_s	Scattering vector
k_z	Effective vertical interferometric wavenumber
l	Physical length of the radar antenna
L_{SA}	Length of the synthetic aperture
R	Slant range distance from the radar to a target
r_A	Azimuth resolution
r_{GR}	Ground-range resolution
r_{SR}	Slant-range resolution
S	Scattering matrix
s	SAR complex image
v	Along-track radar speed

Chapter 1

Introduction

The need of reliable all-weather monitoring of Earth has driven the development of advanced Synthetic Aperture Radar (SAR) remote sensing techniques. SAR is a variant of radar in which a very long antenna is synthesized using a transported small antenna and signal processing, thereby allowing fine resolution with longer wavelengths. The antenna is usually mounted on an aircraft or a spacecraft from which a target scene is illuminated and the amplitudes and phases of the echoes recorded in a signal history. SAR operates usually in the microwave region of the electromagnetic (EM) spectrum so it is barely affected by cloud cover and atmospheric attenuation. Furthermore SAR is an active sensor, that is, it transmits a signal and measures or records the response returned from the target. That means SAR is independent of solar illumination conditions and capable of collecting data night and day (26).

Good resolution, weather independence and 24 hour operation (spaceborne) make SAR a very valuable tool for the operative monitoring and scientific study of the Earth. It is used in several applications such as observation of ocean currents (18), monitoring of sea ice (7), estimation of forest biomass (45) or to study seismic deformations (44) and volcanic activities (43).

This work studies possibilities to retrieve forest height estimates from spaceborne X-band radar measurements by means of SAR interferometry (InSAR). Height information can be related to forest biomass by using allometry equations (82) and biomass is one of most desired parameters for applications like climate modelling, resource assessment and wood industry. It has been demonstrated that current interferometric techniques applied to airborne SAR images can provide fairly accurate estimates of

tree height (52, 53, 54). However, it is not clear if those methods are equally appropriate for measuring canopy height from space with the latest satellites equipped with SAR.

In this work the ability of the SAR satellites TerraSAR-X and TanDEM-X to estimate tree height is evaluated and compared with the results of the FINSAR campaign (52, 53, 54).

1.1 Structure of the report

This report is divided into 5 chapters. It starts with this introductory chapter where a short overview of SAR history, an introduction to forest biomass measurement with SAR and the thesis objective are presented.

In the second chapter the theory involving basic electromagnetics, SAR, InSAR, SAR Polarimetry (PolSAR) and Polarimetric SAR Interferometry (Pol-InSAR) is exposed.

The third chapter presents the material used for the development of this thesis which includes the study area in southern Finland, the data and the instruments.

In the fourth chapter are detailed the processing steps carried out for data analysis, paying particular attention to the processing of TanDEM-X mission data.

In the fifth chapter, the canopy height information obtained from TanDEM-X data is compared with the results of the FINSAR campaign and with an accurate Digital Elevation Model (DEM) of the terrain and the results are discussed.

In the last chapter a conclusion for the project is presented.

1.2 Brief history of SAR

SAR was firstly developed in the 1950s as a military reconnaissance tool. It emerged as a solution to the United States Army's need for an aerial remote surveillance device that could work regardless of Sun light and in all kind of weather conditions. Radar seemed the logical choice because its ability to penetrate clouds and its non-dependence of available light. However, for achieving high enough resolutions the radar antenna had to be far too big for an aircraft to carry. The problem was solved by the introduction of the synthetic aperture.

The concept of synthetic aperture was developed in the United States in 1951 by Carl Wiley (41), from the Goodyear Aircraft Corporation. Wiley noticed that each object in a scene illuminated by radar has a different relative speed to the antenna and as a result, each signal reflected in a different object has its own Doppler shift. He concluded that analysing the frequency of the reflections, fine resolution images can be obtained (79).

After this finding, Goodyear Aircraft continued research in SAR technology and introduced several advancements during the 1950s and the 1960s (14). However they were not the only ones developing SAR. In 1952, researchers at the University of Illinois started to work independently on SAR technology and developed the concept of beam-sharpening. They demonstrated it experimentally using airborne X-band pulsed radar and generating the first strip-map image (62). In 1953, the University of Michigan started to work on another SAR project called *project Michigan* that laid the foundations for practical SAR (4, 5, 6). They proposed to consider not just the short-term existence of several particular Doppler shifts but the entire history. The processing demands to carry out that exceeded the limits of the analog processors of the day. The problem was solved by optical processing of the data and in 1957 the group produced the first SAR imagery. The interest on SAR grew and other institutions also started to explore this technology.

In 1974, engineers from the Jet Propulsion Laboratory (JPL) of the National Aeronautics and Space Administration (NASA) formed an alliance with international scientists of the National Oceanic and Atmospheric Administration (NOAA) in order to explore the possibilities of space-based SAR for ocean observation. SAR can collect data independently of sun light and weather conditions and it is sensitive to small surface roughness changes due to its operating wavelengths. This makes it very suitable for obtaining ocean information such as surface waves, internal waves, currents, sea ice or wind. NASA/NOAA efforts culminated in June of 1978 with the launch of the SEASAT (32) satellite. SEASAT was the first spaceborne SAR and provided a powerful new tool for studying the Earth. It operated until October of 1978, when it experienced a massive short circuit in the power system.

Despite the progress made with the SEASAT, it was not until the 1990s when there was a real expansion of SAR space missions. In 1990, NASA started a mission for mapping the surface of Venus using SAR on board of the Magellan spacecraft (60).

The mission lasted 4 years and meant the first interplanetary utilization of SAR. On the other hand, five SAR satellites were placed in orbit for earth observation. These satellites were Soviet ALMAZ (35) (1991) , Japanese JERS-1 (46) (1992) , European ERS-1 (11) (1991) and ERS-2 (12) (1995) and Canadian RADARSAT-1 (56) (1995).

Nowadays, SAR is a consolidated and valuable tool for remote sensing and many scientific satellites such as ESA's ENVISAT (10) or German Aerospace Center (DLR) TerraSAR-X (TSX) (73) and TanDEM-X(TDX) (22) are equipped with it. Capable of working with a wide range of resolutions and independently of solar light and weather conditions, SAR is used for numerous applications ranging from topographic mapping to environmental and climate monitoring.

1.3 Forest biomass measurement with SAR

Before space platforms could provide the well-defined orbits and short baselines necessary for InSAR (see section 2.4), forest biomass was related to the intensity of SAR backscattering (28, 33, 55). This relation is especially strong for longer wavelengths and can provide some information about the biomass. The launch along the 1990s of ERS-1 (1991), JERS-1 (1992), RADARSAT-1 and ERS-2 (1995) allowed interferometric techniques to start providing accurate forest height measurements and , accordingly, more accurate biomass estimates (16, 27, 29, 31, 72).

Most of SAR based forest height retrieval techniques rely on model-based InSAR analysis. Traditional coherent forward models (38, 39, 40, 65, 66, 80) provide a good insight into the expected behaviour of the forest canopies but they require numerous input parameters. Common methods use several independent observations through multi-polarization, multi-frequency, multi-incidence angle, and multi-baseline acquisitions (69, 70), as well as supplementary topographic information. Other options use simpler models for data interpretation. For instance, inversion of Pol-InSAR data using the Random Volume over Ground (RVoG) model (3, 49, 50, 68, 71) provides reliable estimates of the forest height. In theory this model is applicable only to Pol-InSAR data but results from the FINSAR campaign (52, 53, 54) showed that X-band single polarization interferometric coherence can be successfully used to retrieve forest height under certain conditions.

1.4 Objective

The objective of this work is to evaluate spaceborne TSX and TDX satellites capability to map forest height applying interferometric techniques. In order to do that, forest scattering center location in TanDEM-X interferometric images is studied and compared with the results achieved in works with E-SAR airborne SAR data (52, 53, 54).

Chapter 2

Theoretical background

In this chapter, the theoretical background of this thesis is presented. It covers some basic electromagnetic theory and the fundamentals of Synthetic Aperture Radar. The review is mostly based on the books (9) and (26).

2.1 Overview of EM waves

This section provides a brief look at the theory of EM waves formulated by the Scottish physicist James Clerk Maxwell in 1873. In addition it states the most important parameters concerning EM waves that are of interest for SAR remote sensing.

2.1.1 Electromagnetic waves

An EM wave is a form of energy emitted and absorbed by charged particles which propagates in wave form through vacuum or through some medium characterized by certain physical constants. Electromagnetic waves are formed by an electric field vector $\vec{E}$ and a magnetic field vector $\vec{H}$ perpendiculars to each other and to the propagation direction $\vec{r}$ (Figure 2.1). As it is common, the discussion will be in terms of the electric field $\vec{E}$ but everything can be applied in the same way to the magnetic field.

The sinusoidal solution to the electric wave equation travelling in $\vec{r}$ direction in a lossy and homogeneous medium takes the form

$$E(r,t) = E_0 e^{-\alpha r} \cos(\omega t - \beta r) \tag{2.1}$$

where E_0 is the amplitude, ω_0 is the radian frequency, β is the phase constant and α is the attenuation constant.

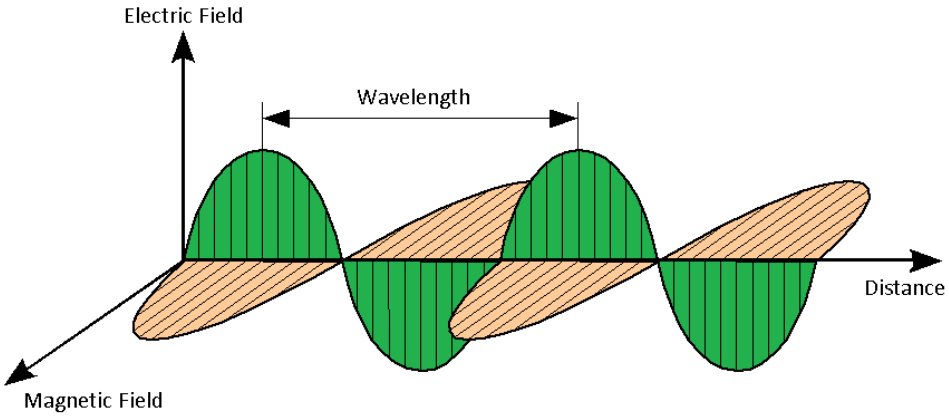

Figure 2.1: EM wave. Adapted from the image available at (78).

2.1.2 Material constants

There are two main parameters of a material that describe its interaction with EM waves: the magnetic permeability μ and the complex electric permittivity ϵ_c. The permeability is the same for all materials of interest in SAR applications as in vacuum and its value is $\mu = \mu_0 = 4\pi \cdot 10^{-7} H/m$ (SI units). The complex permittivity gives the main information about how the medium responds to the presence of an electric field and is defined as

$$\epsilon_c = \epsilon - j\frac{\sigma}{\omega_0} = \epsilon' - j\epsilon'' = \epsilon_0(\epsilon'_r - j\epsilon''_r) \tag{2.2}$$

where ϵ is the absolute permittivity of the material (units of F/m), σ is the conductivity of the material (units of ohms, Ω) and ϵ' and ϵ'' are the real and the imaginary parts respectively of ϵ_c. It is usual to represent ϵ_c as a function of the permittivity of vacuum $\epsilon_0 = 8,85 \cdot 10^{-12} F/m$ and a dimensionless constant known as relative permittivity ϵ_r. Relative permittivity has also a real ϵ'_r and an imaginary ϵ''_r part.

The losses of the material are given by the imaginary part of ϵ_c and are usually

represented in terms of the loss tangent

$$\tan(\delta) = \frac{\epsilon''}{\epsilon'} = \frac{\epsilon_r''}{\epsilon_r'} = \frac{\sigma}{\omega_0 \epsilon} \tag{2.3}$$

If $\tan(\delta) \gg 1$ the material is considered a good conductor and if $\tan(\delta) \ll 1$ the material is considered a good dielectric.

2.1.3 Frequency/wavelength

In a sinusoidal wave, wavelength is the distance between two consecutive points with the same phase (vibrational status) (Figure 2.1) and frequency is the number of oscillations per seconds. They are interrelated as

$$\lambda = c/f \tag{2.4}$$

where c is the phase velocity in the medium $c = 1/\sqrt{\epsilon\mu}$ that in vacuum and in air is $c = c_0 = 3 \cdot 10^8 m/s$ (speed of light). It is common to denote the wavelength by the wave number

$$k = \frac{2\pi}{\lambda} \tag{2.5}$$

2.1.4 Attenuation and penetration depth

The attenuation coefficient of a material can be expressed as

$$\alpha = k\sqrt{\frac{1}{2}\sqrt{(1 + (\tan^2(\delta)) - 1)}} \tag{2.6}$$

and gives information about how rapidly an EM wave is attenuated in the medium. On the other hand the penetration depth is defined as

$$\delta = \frac{1}{\alpha} \tag{2.7}$$

and tells how deep an incident EM wave penetrates into the medium.

2.1.5 Polarization

The polarization of an EM wave is determined by the geometric figure described by the end of the electric field vector at a given point in space during one oscillation period. If the described figure is a straight line the wave is linearly polarized, if it is a circle then the wave is circularly polarized and if it is an ellipse then the wave is elliptically polarized (Figure 2.2). For circular and elliptical polarizations it is also defined the concept of handedness which indicates the sense of rotation of the electric field vector of a wave travelling away from the observer. If the rotation is clockwise the wave is right-handed and if the rotation is anticlockwise the wave is left-handed.

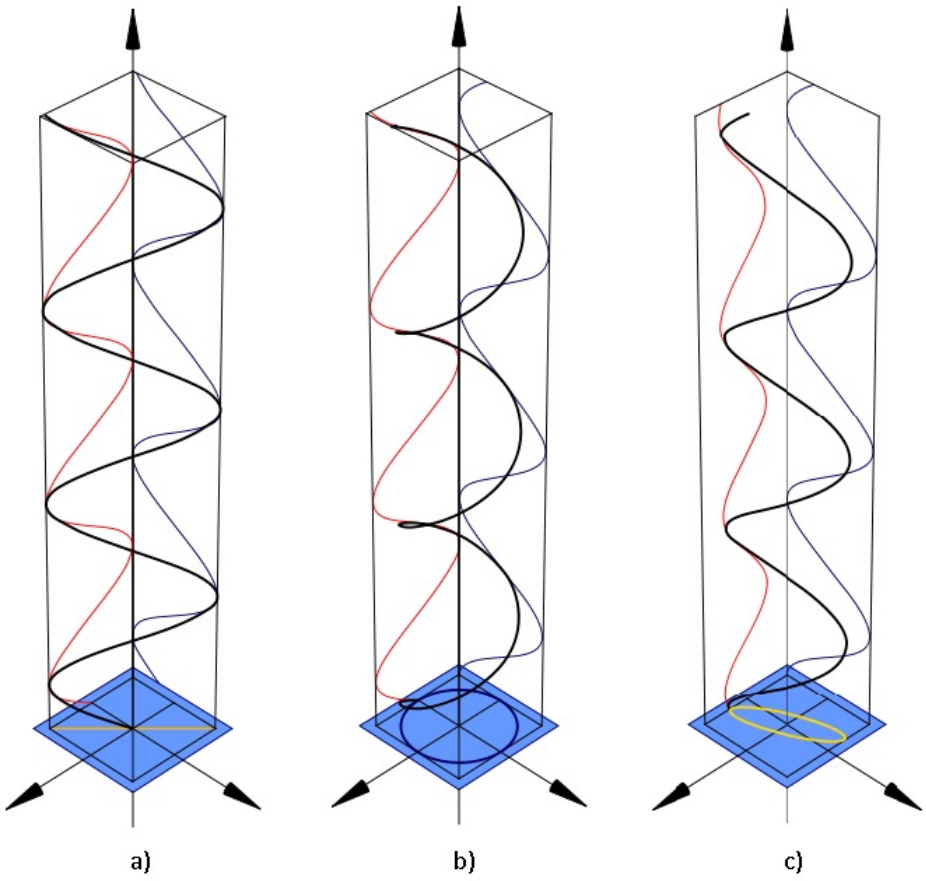

Figure 2.2: Polarization types. Diagrams of linear (a), circular (b) and elliptical (c) polarizations. Images from (74, 75, 76).

2.2 SAR

This section presents a theoretical description of SAR basic operating principles, geometry, variables and processing. It also discusses the main parameters of targets concerning SAR imaging.

2.2.1 Overview of SAR systems

A typical SAR system consists of a radar mounted on an airborne or a spaceborne platform and a signal processor. The radar antenna is pointed perpendicular to the motion vector of the moving platform and transmits pulses of radio waves or microwaves which are scattered by any object in their path. The object reflects back a tiny fraction of the incident field and this is measured by the receiving antenna, which is usually placed at the same site as the transmitter. In the receiver the signal is filtered, amplified and recorded coherently, that is, amplitude and phase as a function of time. A scheme of a typical SAR system is represented in Figure 2.3.

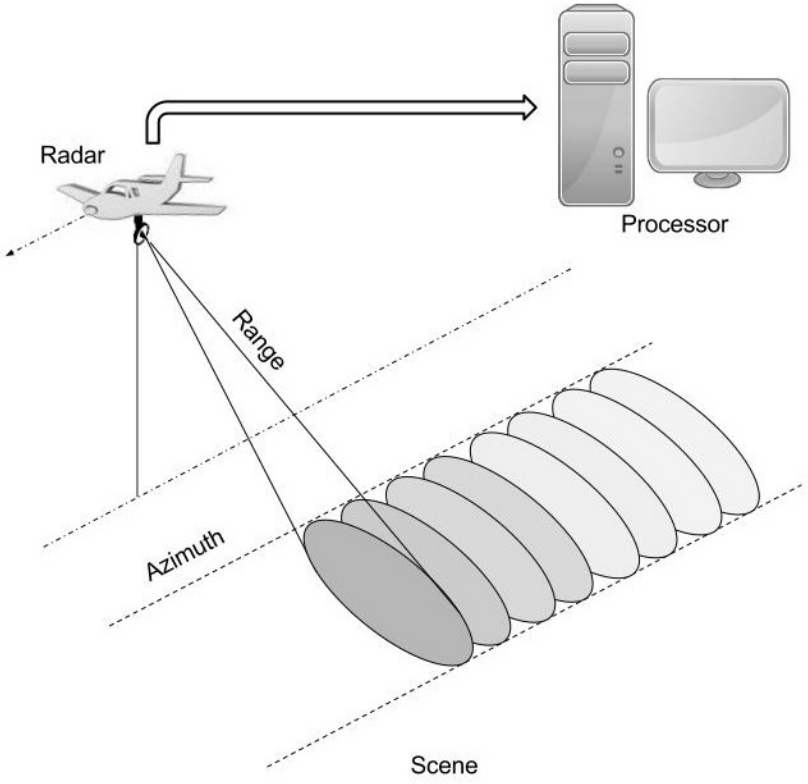

Figure 2.3: Essential elements of a typical SAR system.

The task of the processor is to convert the stored data into a two-dimensional (2D) image in which the brightness of each pixel represents the intensity of the reflected signal. One dimension of the image is called range and is a measure of the line-of-sight distance from the radar to the target. Range is determined by precisely measuring the time between the transmission of the pulse and the reception of the echo from a target. The other dimension is called azimuth and is a measure of the along track distance from the radar to the target. Azimuth distances are obtained by a Doppler approach. The ability of SAR to produce fine azimuth resolution differentiates it from other imaging radars. In Figure 2.4 an exemplary SAR image is shown.

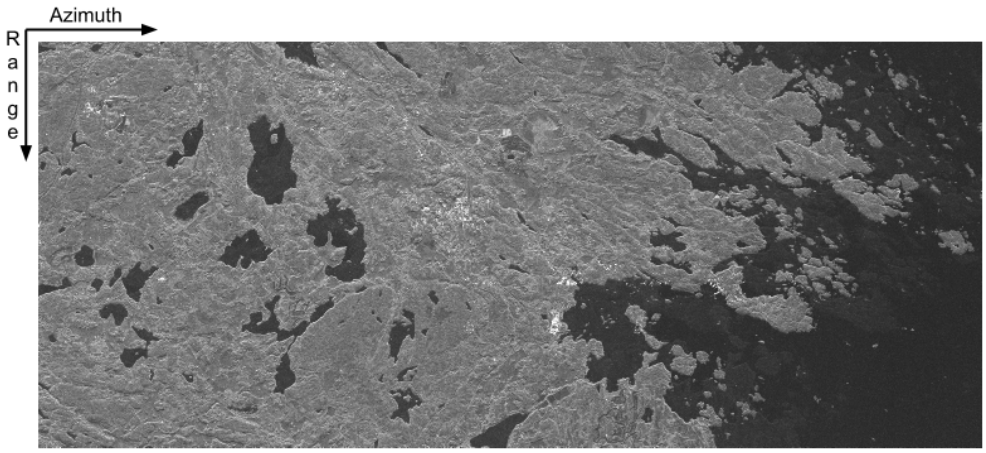

Figure 2.4: TDX SAR image of southern Finland.

2.2.2 Concept of synthetic aperture

Obtaining fine azimuth resolution requires a physically large antenna to focus the transmitted and received energy into a narrow beam. The need for a large antenna is often referred as the need for a large aperture in allusion to optical systems in which large apertures (lenses or mirrors which are analogous to the radar antenna) are required to obtain fine resolution.

SAR produces fine resolution images by simulating a very long antenna, more specifically a very long one-dimensional phased array of antennas. The main difference between a phased array and SAR is that in a phased array several antennas receive at the same time while in SAR a single physical antenna gathers signals at different posi-

tions and at different times, taking advantage of the fact that the target is essentially stationary during the acquisition time. This is called synthetic aperture (Figure 2.5).

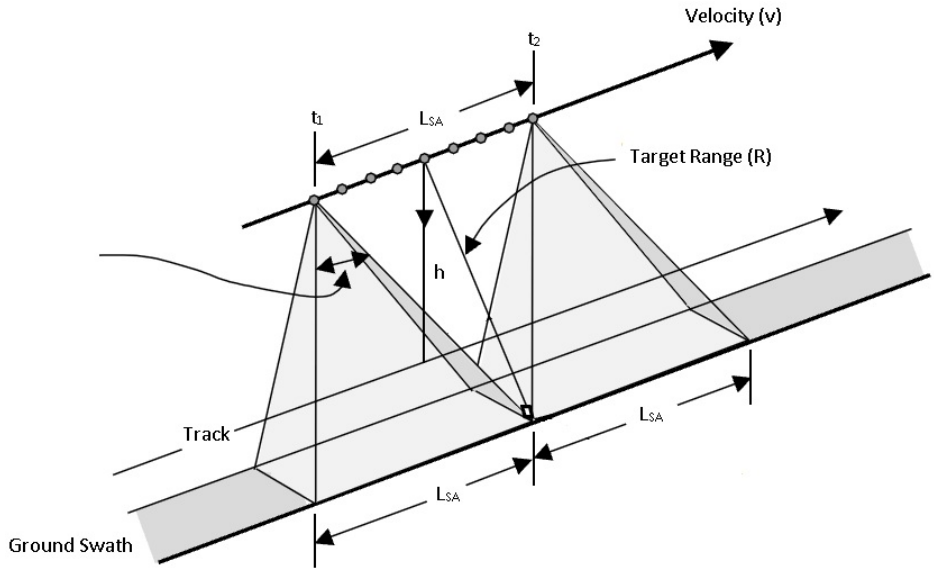

Figure 2.5: Geometry showing the formation of a synthetic array by moving a single antenna along a track.

Since SAR is a coherent system mounted on a moving platform with a side-looking antenna, the received signals have an appreciable frequency shift due to the Doppler effect. This frequency shift is positive when the target enters the beam, it decreases down to zero, and then it becomes increasingly negative while the target is exiting the beam (Figure 2.6). The spectrum of the echo covers the region $f_0 \pm f_D$, where f_0 is the frequency of the transmitted signal and f_D is the Doppler frequency shift. The range within the received signals frequency may vary is known as the Doppler spectrum of the system and its bandwidth is $B_D = 2f_D$. The Doppler frequency shift is given by

$$f_D = \frac{2v}{\lambda}\sin(\frac{\theta}{2}) \approx \frac{v\theta}{\lambda} \tag{2.8}$$

where v is the relative velocity along the radar line-of-sight, λ is the radar wavelength and θ is the angular location of the target (within the antenna beam) with respect to the zero-Doppler plane. The zero-Doppler plane is defined as the plane orthogonal to the velocity vector of the vehicle transporting the radar.

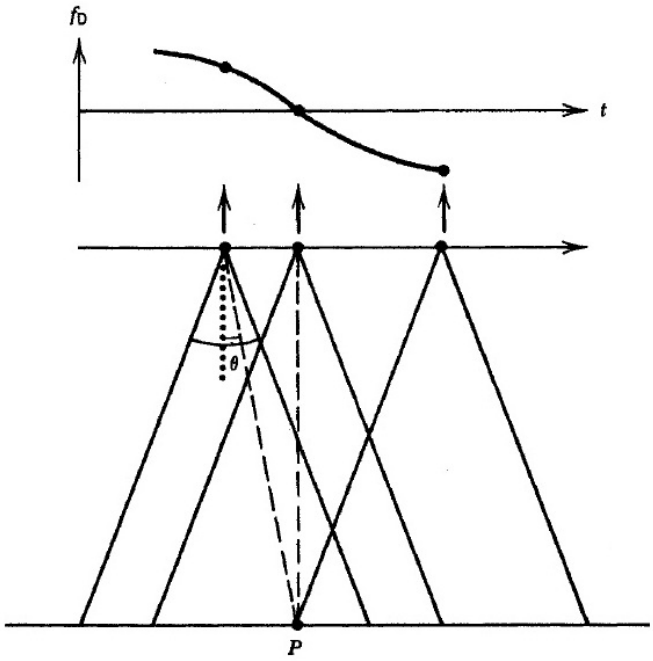

Figure 2.6: Doppler history of a point target as the sensor passes by. Image from (9).

The distance along the flight track during which a scatterer is illuminated is defined as the length of the synthetic aperture L_{SA} (see Figure 2.5).

2.2.3 SAR parameters

In this section the main parameters concerning SAR and its influence in the appearance of the produced imagery are discussed.

2.2.3.1 Incident, look and depression angles

The incident angle θ is defined as the angle between the radar line of sight and the local vertical with respect to the Earth surface. This parameter affects the appearance of the objects in the produced images and also the intensity of the received backscatter, which generally decreases with bigger incident angles. On the other hand, the look angle Φ is the angle between the vertical of the antenna to the ground and the transmitted ray at the point of incidence. Finally, the depression angle β is defined as the angle between the horizontal line of the antenna and the transmitted ray at the point of incidence.

Notice that the main difference between these angles is that look and depression angles does not account for the effects of Earth curvature. In Figure 2.7 are shown these and other angles usually defined in SAR geometry.

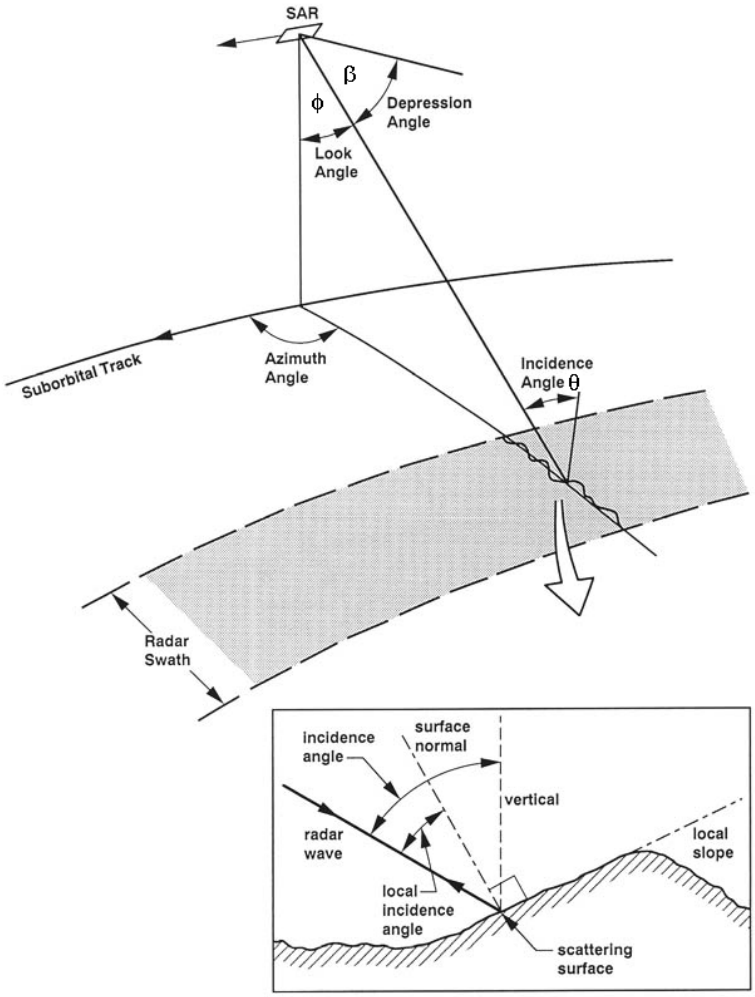

Figure 2.7: Main angles defined for SAR systems. Image from (26).

2.2.3.2 Frequency/wavelength

SAR systems usually operate in a single frequency/wavelength mode within the range of microwaves. The main benefit of using microwaves is that at those frequencies the attenuation of the atmosphere is negligible (Figure 2.8), in other words, the atmosphere is transparent to microwave radiation. The selection of the operating wavelength is

mainly determined by the application (e.g. appearance of vegetation, soil or water surfaces vary depending on the wavelength). Wavelength affects the returned power (Equation 2.6), the dielectric response (Equation 2.2), the penetration depth (Equation 2.7) and the definition of surface roughness (see section 2.2.4.1). Common microwave radar bands are shown in Table 2.1.

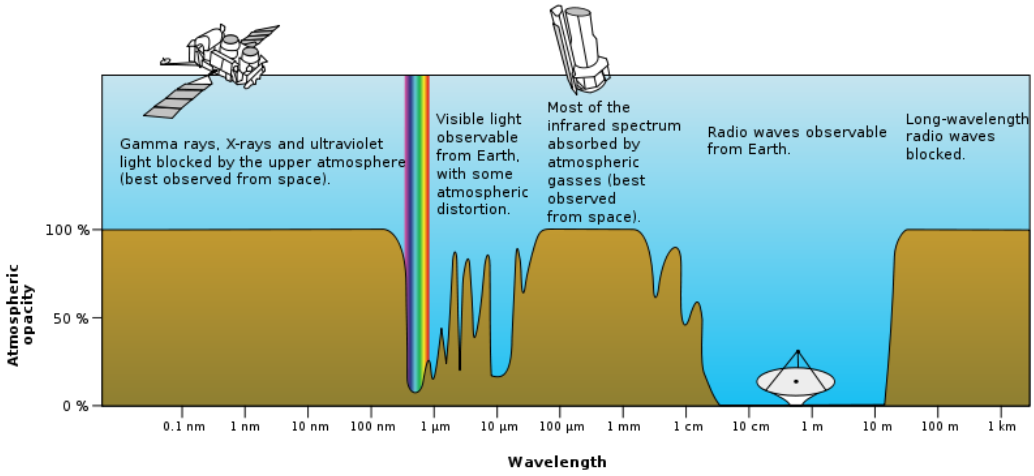

Figure 2.8: Electromagnetic transmittance or opacity of the Earth's atmosphere. Image from (77).

Radar Frequency Band	Wavelength (cm)	Frequency Range (MHz)
P	136 - 77	220 - 390
L	30 - 15	1.000 - 2.000
S	15 - 7,5	2.000 - 4.000
C	7,5 - 3,75	4.000 - 8.000
X	3,75 - 2,40	8.000 - 12.500
Ku	2,40 - 1,67	12.500 - 18.000
K	1,67 - 1,18	18.000 - 26.500
Ka	1,18 - 0,75	26.500 - 40.000

Table 2.1: Frequency Bands of typical remote sensing radars.

2.2.3.3 Polarization

Typically SAR uses vertical or horizontal linearly polarized microwave radiation. The configuration of emitting and receiving polarization is known as the polarization scheme

of the system. In table 2.2 the possible configurations are shown. Generally like-polarized schemes provide a stronger received signal and with better signal to noise ratio than cross-polarized schemes (Figure 2.9.a). That is due to the fact that in a cross-polarized configuration only the part of the transmitted signal that is depolarized can be recorded. HH polarization schemes provides a stronger returned signal if the target have a strong horizontal component and vice versa. On the other hand, cross-polarized schemes usually give more information about randomly oriented surfaces such as vegetation volumes (Figure 2.9.b).

Like-Polarized	
HH	Horizontal Transmit; Horizontal Receive
VV	Vertical Transmit; Vertical Receive
Cross-Polarized	
HV	Horizontal Transmit; Vertical Receive
VH	Vertical Transmit; Horizontal Receive

Table 2.2: Common linear polarization schemes used in SAR remote sensing.

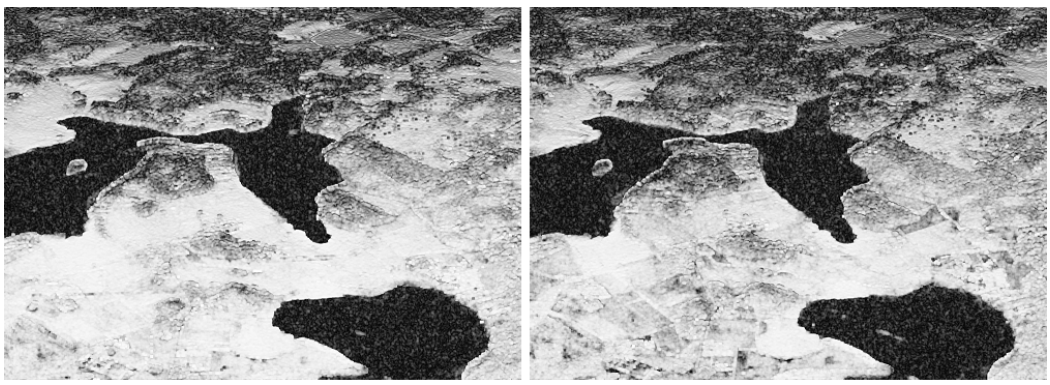

Figure 2.9: L-band SAR images from FINSAR campaign. a) Acquired using HH polarization scheme. b) Acquired using HV polarization scheme.

2.2.3.4 Resolution

Resolution is a key parameter in SAR and its understanding is essential for proper interpretation of SAR images. Resolution provides information about the size of the area responsible of a radar reflection (resolution cell) and defines the minimum separation

between two targets to distinguish one from the other. The range of resolutions of a particular SAR system determines its feasibility for a particular application. In SAR resolution is defined in to directions: perpendicular to the flight path (range resolution) and parallel to the flight path (azimuth resolution) (Figure 2.10).

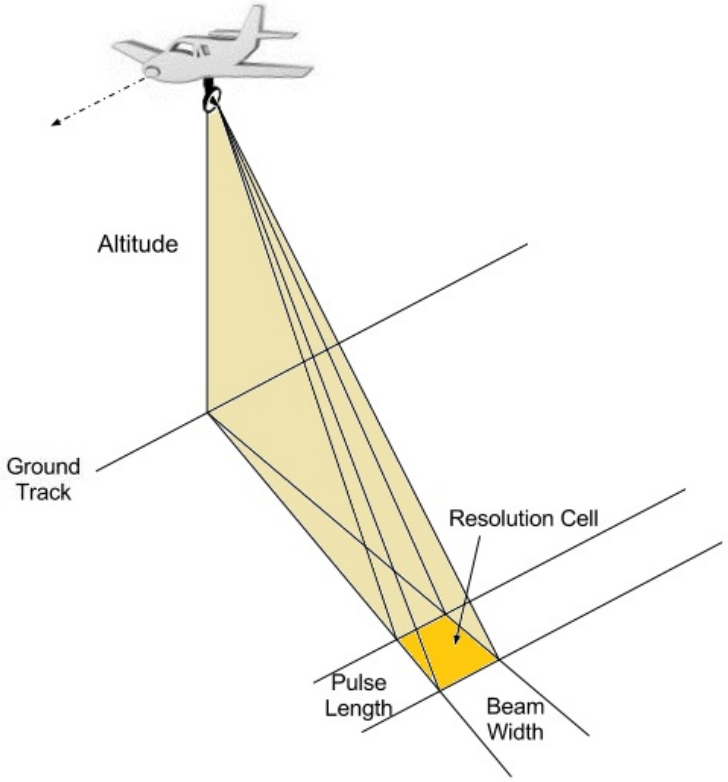

Figure 2.10: SAR system resolution.

Range resolution is directly related to the length of the transmitted pulse τ. The shorter the pulse length, the finer the range resolution of the system. However, the pulse length can not be reduced indefinitely because that also implies decreasing the total energy illuminating the target and therefore that the returned signal would be too weak to be captured. There are two main definitions for resolutions in range direction: slant-range resolution and ground-range resolution. Slant-range resolution is constant across the range and is defined as

$$r_{SR} = \frac{c\tau}{2} \tag{2.9}$$

where c is the speed of light. More relevant than slant-range resolution is ground-range resolution which is not constant across the range and its equation is

$$r_{GR} = \frac{c\tau}{2\sin(\theta)} = \frac{c\tau}{2\cos(\beta)} \tag{2.10}$$

where θ is the look angle and β is the depression angle. It is important to notice the dependence with the look angle. Points closer to the flight path (near range) have worse resolution that points further from the flight path (far range) (Figure 2.11). The selection of the look angle is critical to determine the difference between resolutions at far and near ranges.

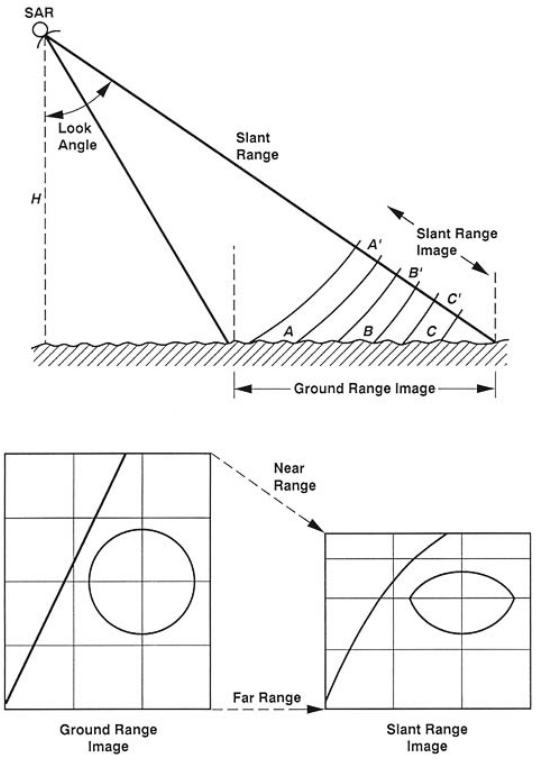

Figure 2.11: Radar range geometry. Image from (26)

On the other hand, azimuth resolution in SAR is directly related to the physical length of the radar antenna l and its equation is

$$r_A = \frac{l}{2} \tag{2.11}$$

Observe that r_A is improved with smaller antennas and is independent of range distance, sensor altitude, look angle and wavelength. However, reducing indefinitely the length of the antenna to improve resolution is not possible due to two main limitations. The first one is that smaller antennas has lower gain which means poorer signal to noise ratio. The second limitation is given by the fact that SAR transmits a series of frequency modulated (FM) pulses instead of a continuous signal. The pulse repetition frequency (PRF) must be high enough to make sure that the Doppler spectrum is sufficiently well sampled in order to do the processing (Figure 2.12). The used criteria is that the transmitter must send at least a pulse each time the antenna moves half its length (67). This is equivalent to

$$PRF > \frac{v}{l/2} \tag{2.12}$$

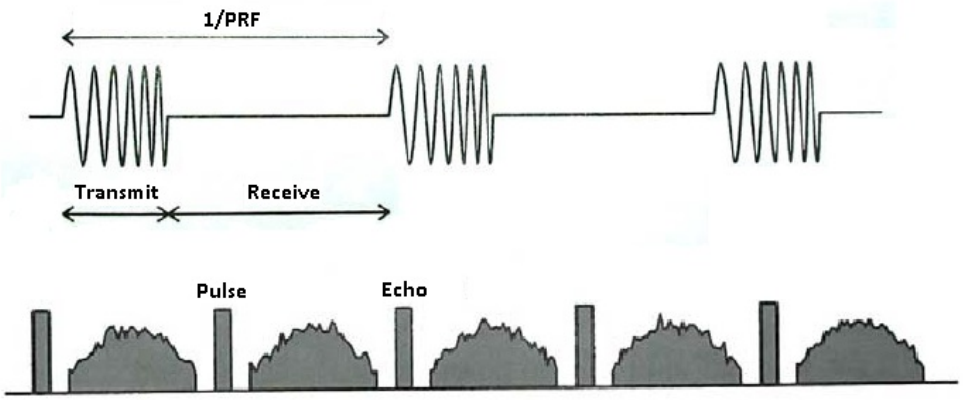

Figure 2.12: Pulse transmission in SAR. Adapted from the image available at (8).

Therefore, if the antenna length is decreased resolution is improved but high power transmitters are needed and the radar must pulse faster.

2.2.4 Target parameters

In addition to SAR parameters, there are three main target parameters that need to be considered in order to understand SAR imaging: surface roughness, dielectric constant and local incident angle.

2.2.4.1 Surface roughness

The roughness of a target determines its interaction with incident EM waves. A surface is considered rough or smooth depending on the wavelength of the incident radiation. If $\lambda \gg surfaceroughness$ then the surface is considered smooth and behaves like a specular reflector governed by Snell's law, that is, the angle of reflection is equal to the angle of incidence (Figure 2.13.a). On the other hand, if emph$\lambda \ll surfaceroughness$ the surface is considered diffuse and the incident energy is reflected isotropically, that is, equally in all directions (Figure 2.13.d). Between those extreme cases both specular reflection and diffusion are present (Figure 2.13.b and 2.13.c). As a surface gets rougher, the reflected energy becomes more diffuse and less governed by Snell's law and vice versa. To determine when a surface starts to behave diffusely the Rayleigh criterion is used. Rayleigh stated that a surface is smooth if

$$h < \frac{\lambda}{8\cos(\theta)} \tag{2.13}$$

where h is the Root Mean Square (RMS) height of the surface and θ is the incident angle of the EM wave. Only rough surfaces causes backscatters that can be measured and recorded by the radar.

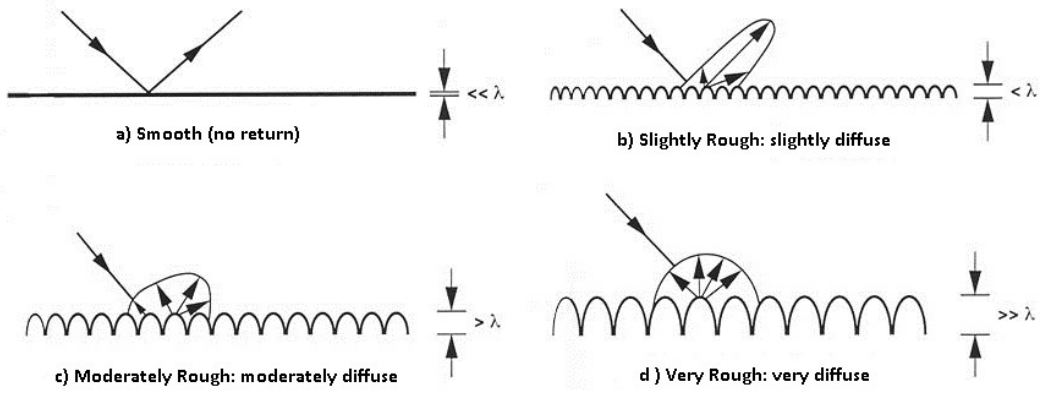

Figure 2.13: Specular reflection and diffuse scattering. Specular reflection and diffuse scattering from smooth (a) and rough (b, c, d) surfaces. Adapted from the image available at (26).

2.2.4.2 Dielectric constant

Dielectric constant affects the absorption and propagation of electromagnetic waves and consequently the interaction of electromagnetic radiation with the target surface. Complex dielectric constant is frequency dependant (Equation 2.2) and basically affects two parameters of a target: the reflectivity, which is the fraction of incident radiation reflected by the surface, and the penetration depth.

At radar frequencies, the complex dielectric constant of most natural materials, when dry, is between 3 and 8. For such values, the penetration depth is fairly large and the reflectivity small. On the other hand, for water the dielectric constant is around 80 (for the same frequencies) which results in high reflectivity from the surface and almost no penetration. The complex dielectric constant for a material varies almost linearly with the moisture content per unit of volume (Figure 2.14). The higher the moisture content, the lesser the penetration depth and the greater the reflectivity. The observed variation in reflectivity from natural surfaces is mainly due to its moisture content. Thus an analysis of the returns for a specific region allows for example the classification of the type of soil or vegetation being imaged.

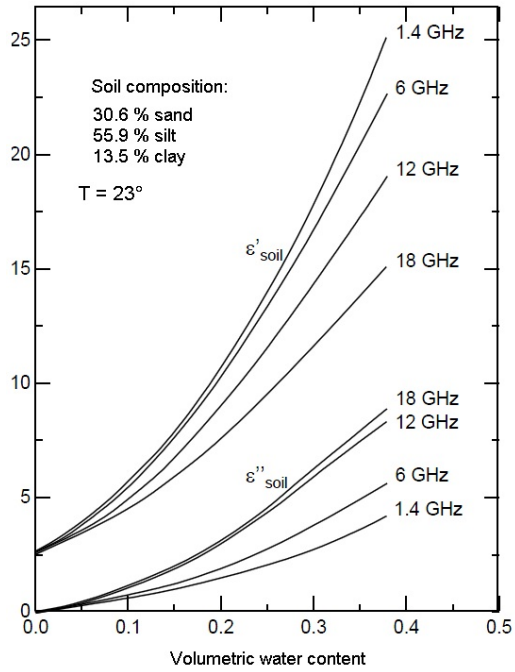

Figure 2.14: Soil permittivity variation due to water content and frequency.

As mentioned, the dielectric constant depends on the frequency of the EM wave. The higher the frequency (or the lower the wavelength), the lesser the penetration is. For instance, using a high frequency for imaging a forest will result in surface scatter from the top of the vegetation canopy while a lower frequency would allow the EM waves to penetrate the canopy, producing volume scattering from the leaves, branches, trunks or ground.

2.2.4.3 Local incident angle

The local incident angle is defined as the angle between the radar line-of-sight to certain point on the target under study and the normal to the tangent plane at that point (Figure 2.7). This parameter has two main effects on the SAR image. On the one hand, the brightness of the point strongly depends on the local incident angle. For instance if the slope of a mountain is perpendicular to the radar beam, the energy reflected back to the radar will be greater that in the case of a flat land. On the other hand, several geometric distortions can appear on the image due to the local incident angle or slope of a point. These distortions will be reviewed in detail in the section 2.2.6.2.

2.2.5 SAR processing

The signal energy retrieved from a point target is spread in range by the duration of the transmitted pulse and in azimuth by the length of the synthetic aperture. SAR processing is a two-dimensional problem in which that disperse energy has to be focused into a single pixel in the output image (Figure 2.15). Thus, the purpose of the SAR processor is to produce a focused image by operating on the signals recorded by the radar. There are several SAR processing algorithms but the most representative and commonly used is the Range/Doppler algorithm (RDA).

2.2.5.1 Range/Doppler algorithm

As a point target passes through the azimuth antenna beam, the distance to a target changes causing a phase variation in the received signal as a function of azimuth. This phase variation over the synthetic aperture corresponds to the Doppler bandwidth of the system and allows the signal to be compressed in the azimuth direction. However,

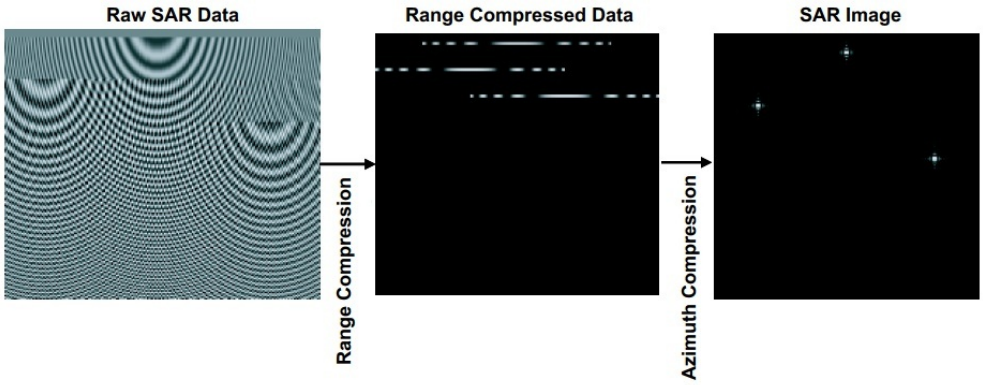

Figure 2.15: SAR focusing in range and azimuth. Image from (9).

nearly all objects illuminated by the antenna have an angular orientation with respect to the radar that is different from the antenna boresight pointing angle. That means that the signal data from a scatterer has larger delays and appears at larger ranges for azimuth positions away from the azimuth of zero-Doppler (Figure 2.16). This effect is named range (cell) migration and must be corrected before azimuth compression can occur. The Range/Doppler algorithm performs this correction very efficiently.

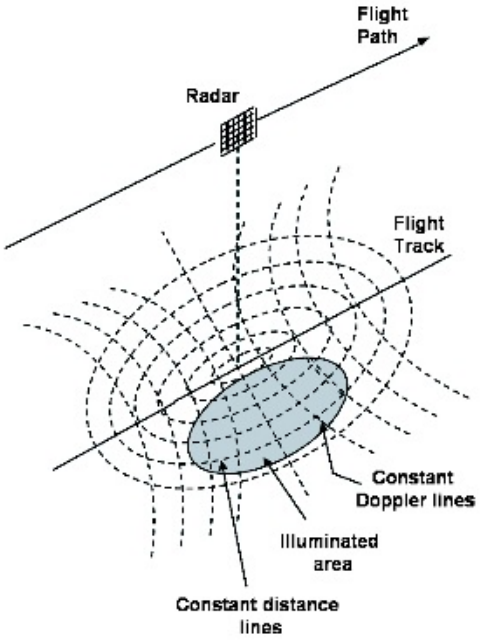

Figure 2.16: Equal Doppler and range lines in SAR imaging. Image from (9).

RDA has 4 main steps: range compression, azimuth Fast Fourier Transform (FFT), Range Cell Migration Correction (RCMC) and azimuth compression (Figure 2.17).

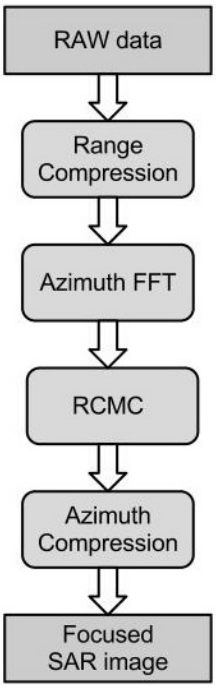

Figure 2.17: Range Doppler algorithm block diagram.

- **Range compression:** Range compression is performed by applying FFT and a matched filter to each range line. Radar transmits linear FM pulses which have the property that when filtered with a matched filter, the result is a narrow pulse in which all the pulse energy has been collected to the peak value. After the matched filtering, an inverse FFT (IFFT) is applied to each line to get the range compressed data. For last, the range compressed data is multiplied by a vector that corrects effects on the amplitude caused by the elevation beam pattern and range spreading loss.

- **Azimuth FFT:** at this step of the RDA, a FFT is performed in the azimuth direction on each range line to transform the data into the range Doppler domain.

- **RCMC:** at this step the main objective is to correct the range migration effect stated above. This effect depends on the zero-Doppler range and on the angle from

the radar to the target relative to the zero-Doppler direction. Targets at the same zero-Doppler range pass through the antenna beam traversing the same interval of angles so they have the same variation in range from the radar. Accordingly, the trajectories of the signals from those targets have the same shape but are displaced in azimuth (Figure 2.18.a). Because of the relationship between the radar-to-target angle and Doppler frequency, the range migration of all targets at the same zero-Doppler range can be expressed as a function of Doppler frequency. This allows RCMC to be performed very efficiently in the range-Doppler domain (Figure 2.18.b). The shift in range needed to align the signal trajectory in a single range bin is determined independently for each azimuth frequency bin. Then the shift is implemented by an interpolation in the range direction.

- **Azimuth compression:** the last step consists of a matched filtering of the azimuth signal, performed efficiently using FFT. Note that at this point the azimuth FFT has already been performed. The frequency response of the matched filter is precomputed using geometry parameters and range. The data is divided into range invariance regions and the same matched filter is applied over a range interval. In addition, an amplitude weighting is performed to control sidelobes in the azimuth impulse response. For last, an IFFT is applied to each azimuth line and a focused SAR image is obtained as a result.

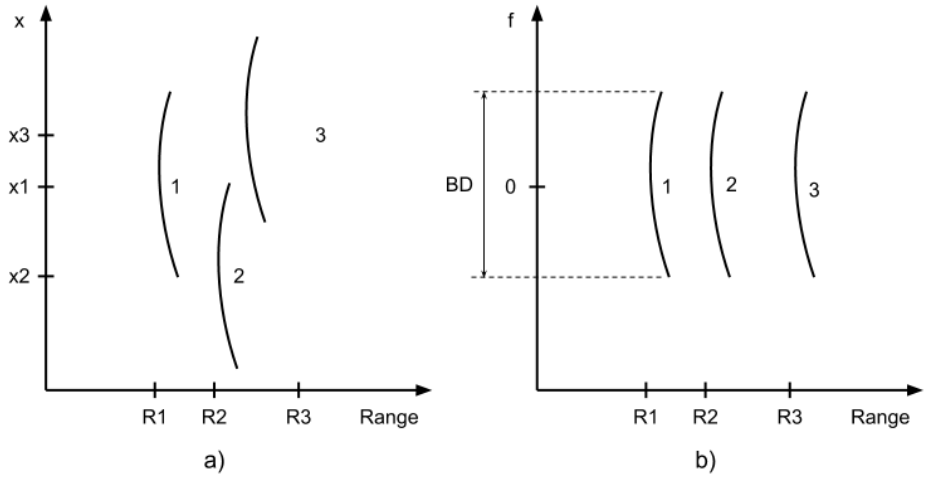

Figure 2.18: Three typical SAR reflected signals. a) In the signal domain. b) In the frequency domain. Adapted from the image available at (26).

2.2.6 Image distortions

Due to the side-looking geometry and to the fact that radar is fundamentally a distance measuring device, some geometric distortions appear on SAR images. There are two main types of these distortions: slant-range scale distortions and relief displacement distortions.

2.2.6.1 Slant-range scale distortion

Slant-range scale distortion occurs since the radar is measuring the distance to targets in range from the radar rather than the true horizontal distance along the ground. This results in a varying image scale moving from near to far range. As it can be appreciated in (Figure 2.11), targets in the near range appear compressed relative to the far range.

Given the geometry of Figure 2.19 and applying basic trigonometrical relationships, ground-range distance can be calculated as

$$G_R = \sqrt{R^2 - H^2} \tag{2.14}$$

where R is the slant-range distance and H the platform altitude. The ground range distance between 2 objects may also be calculated as

$$G_r = H(\cot(\beta_2) - cot(\beta_1)) \tag{2.15}$$

where β_1 and β_2 are the depression angles at the points under study.

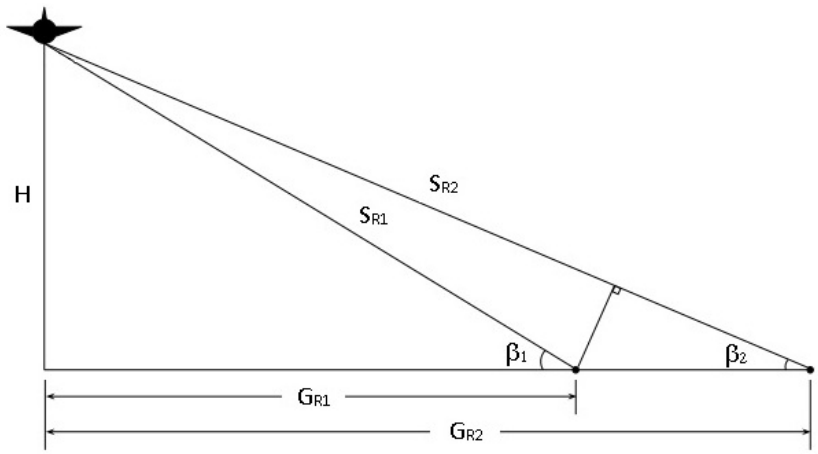

Figure 2.19: SAR range geometry. Adapted from the image available at (26).

2.2.6.2 Relief displacement distortions

The term relief displacement refers to geometric distortions typically associated with tall objects (such as mountains) which get displaced towards the sensor due to their geometry relative to the radar. This displacement is one-dimensional and occurs perpendicular to the flight path. Foreshortening, layover and shadowing are three consequences which result from relief displacement. The appearance of this distortions in SAR images is shown in Figure 2.20.

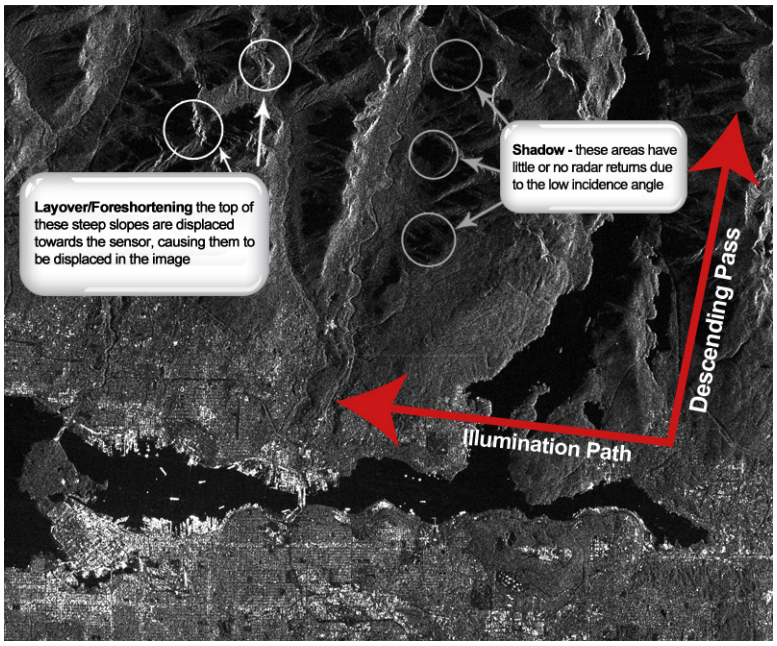

Figure 2.20: SAR image presenting relief displacement distortions. Image from (51).

- **Foreshortening:** in SAR the slant range distance determines the sequence in which targets are displayed and the period of time during which a target is illuminated determines its length on the SAR image. This phenomenon is referred to as foreshortening and results in the shortening of terrain slopes on radar images. This effect is illustrated in Figure 2.21.a.
- **Layover:** this distortion occurs when the radar beam reaches the top of an object before it reaches the base. In that case the return signal from the top will be received before the signal from the bottom. As a result, the top of the object is

displaced towards the radar from its true position on the ground and "lays over" the base of the feature (Figure 2.21.b). Layover effects are more severe for small incidence angles, at the near range and in mountainous terrain.

- **Shadowing:** due to the fact that the radar beam is at an angle, there will be a region of the ground surface behind vertical structures (e.g. mountains) that the beam cannot reach. Since the radar beam does not illuminate the surface, shadowed regions will appear dark on an image as no energy is backscattered. In addition, shadow effects are more notable in far range than in near range because the greater incidence angles (Figure 2.21.c).

2.2.7 Speckle

When a surface is illuminated by a radar EM wave, according to diffraction theory, each point on the illuminated surface acts as a source of secondary spherical waves. Thus, the returned field is the result of the interference of many waves of the same frequency in phase and out of phase. If the surface is rough enough to create path-length differences greater than one wavelength (phase changes greater than 2π), the amplitude and hence the intensity of the retrieved signal varies randomly. This variation in the intensity of backscatters is known as speckle and gives a grainy appearance to radar images (Figure 2.22.

Speckle can be minimized by multi-look filtering or alternately by applying adaptive filters. Applying speckle filters enhances radiometric resolution at the expense of spatial resolution. Although speckle is generally considered an undesired effect, a good interpreter can use its presence or absence as a clue in identifying many terrain features such as land cover types or rock types.

2.2.8 Geocoding

Geocoding refers to the coordinate transformation of a SAR image from the SAR coordinates (range, azimuth, height) to coordinates in a convenient geodetic reference system such as the World Geodetic System 84 (WGS-84) and projection such as Universal Transverse Mercator (UTM). As introduced in section 2.2.6, SAR side looking geometry entails several geometrical distortions such as foreshortening or layover. These

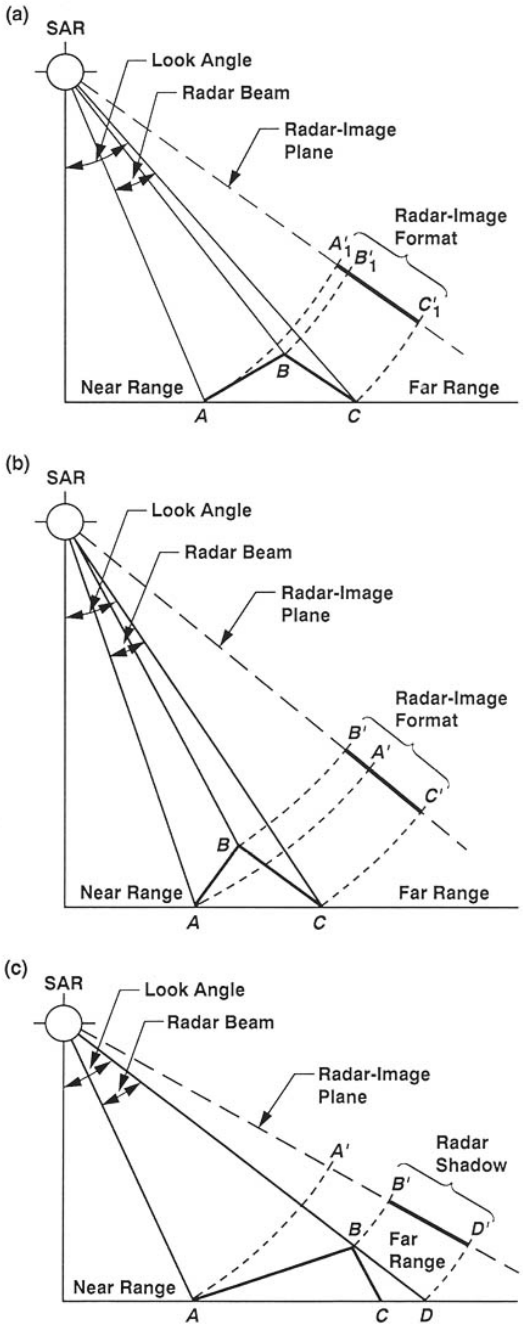

Figure 2.21: Relief displacement distortions in SAR images. a) Foreshortening, where the slope facing the radar is compressed to segment $A' - B'$ while the backslope is extended to segment $B' - C'$. b) Layover, an extreme case of foreshortening where the top of the mountain (B') is imaged before the bottom (A'). c) Shadowing, where the backslope of the mountain ($B' - D'$) is not illuminated by the radar, and no data is acquired. Image from (9).

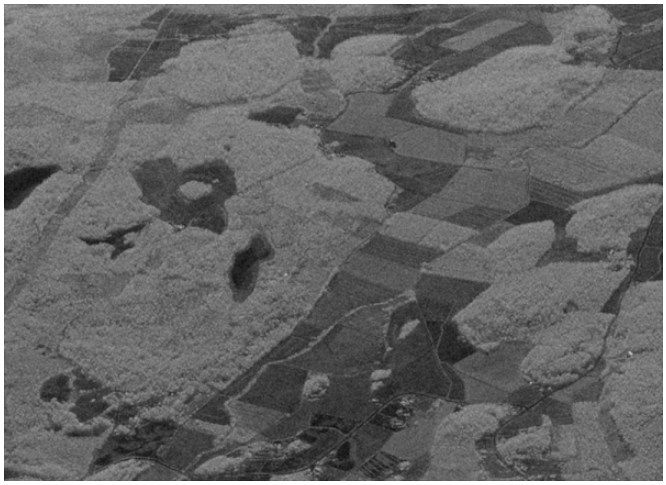

Figure 2.22: L-band SAR amplitude image over forest and agricultural lands in southern Finland.

effects can be corrected with the help of a DEM during the geocoding process. This process implies numerous pixel operations such as pixel averaging that may cause the loss or distortion of the phase information. For that reason, geocoding is usually the last step of any SAR processing.

According to (58), three approaches can be applied to geocode SAR images:

- **Rigorous Range Doppler Approach:** in order to determine the position in the output image (northing, easting, height coordinates) of the pixels on the SAR image (azimuth, range coordinates), this approach performs a complex process in which the relationship between the sensor, each single backscatter element and their relative velocities is calculated. For that, it carries out a complete reconstruction of the imaging and processing procedures by considering the illuminating geometry, the processor characteristics, the geometric distortions and even the influence of Earth rotation and terrain height.

- **Three-dimensional (3D) Interpolative Approach:** in this approach a grid of points (easting, northing, height) is generated and the corresponding pixel coordinates (azimuth, range) of the input image are determined using the rigorous Range-Doppler approach. Then starting from the azimuth and range coordinates at a reference elevation, correction terms in azimuth and range are interpolated

using the individual height values from the DEM. The main purpose of the interpolative approach is to reduce the computing time for generating a terrain corrected geocoded product.

- **Interpolative Ellipsoid Correction:** variation of the 3D interpolation approach in which a net of points is transformed by applying the rigorous range-Doppler-approach.

Common to all cases is the backward geocoding, that is, the output (DEM) is the starting point. In Figure 2.23 is shown a TSX image in slant range coordinates and its geocoded version in the UTM coordinates system.

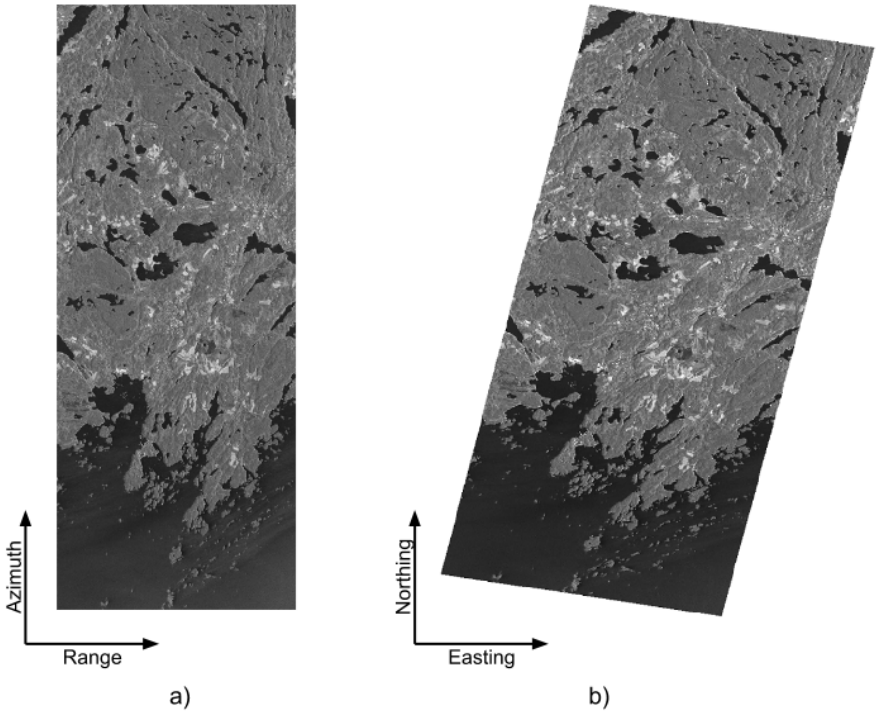

Figure 2.23: TSX SAR image. a) Slant range geometry. b) UTM geographical coordinates.

2.3 SAR Polarimetry (PolSAR)

SAR polarimetry is a technique that uses the existing relationship between the polarization of the incident EM wave on a target and the polarization of the scattered

wave returned from it in order to extract physical parameters and characteristics of the illuminated object or scene. As mentioned early in this chapter, SAR typically uses vertically or horizontally polarized microwave radiation.

2.3.1 The scattering matrix

The scattering matrix mathematically relates the EM wave incident on a target with the EM wave scattered from it. From this matrix the scattering characteristics of the illuminated scene can be extracted.

Supposing that the incident $\vec{E^i}$ and the scattered $\vec{E^s}$ electric fields on a target are determined by the following equations

$$\vec{E^i} = E_h^i \hat{u}_{hi} + E_v^i \hat{u}_{vi} \tag{2.16}$$

$$\vec{E^s} = E_h^s \hat{u}_{hs} + E_v^s \hat{u}_{vs} \tag{2.17}$$

where the phase is not considered and $\hat{u_h}$ and $\hat{u_v}$ are unit vectors perpendicular to each other and to the propagation direction and given these fields in matrix notation

$$\vec{E^i} = \begin{bmatrix} E_v^i \\ E_h^i \end{bmatrix} \tag{2.18}$$

$$\vec{E^s} = \begin{bmatrix} E_v^s \\ E_h^s \end{bmatrix} \tag{2.19}$$

the relationship between the incident and the reflected electric fields is

$$\vec{E^s} = \frac{e^{-jkR}}{R} \cdot S \cdot \vec{E^i} \tag{2.20}$$

where R is the range distance between the antenna and the target, k is the wavenumber and S is the scattering matrix. The R^{-1} term represents the spherical nature of the EM wave and quantifies the attenuation in the propagation direction. On the other hand, the exponential term represents the delay between the target and the radar.

The scattering matrix is defined as

$$S = \begin{bmatrix} S_{hh} & S_{hv} \\ S_{vh} & S_{vv} \end{bmatrix} \tag{2.21}$$

where each term S_{rt} is a complex number representing the relationship between the transmitted field with polarization t and the received field with polarization r. For instance, S_{vh} represents the complex relationship between the horizontally polarized transmitted field and the vertically polarized received field.

Once defined the scattering matrix, Equation 2.20 will be as follows

$$\begin{bmatrix} E_v^s \\ E_h^s \end{bmatrix} = \frac{e^{-jkR}}{R} \cdot \begin{bmatrix} S_{hh} & S_{hv} \\ S_{vh} & S_{vv} \end{bmatrix} \cdot \begin{bmatrix} E_v^i \\ E_h^i \end{bmatrix} \tag{2.22}$$

It is also common to represent the scattering matrix as vector named scattering vector

$$k_s = \begin{bmatrix} S_{hh} \\ S_{hv} \\ S_{vh} \\ S_{vv} \end{bmatrix} \tag{2.23}$$

This is needed for second order statistics calculation.

2.4 SAR Interferometry (InSAR)

This section provides an overview of SAR interferometry, which is the main technique applied in this work. First the principles and main concepts of interferometry are introduced and after that, the focus shifts to the generation of Digital Elevation Models (DEMs) through SAR interferometry.

2.4.1 Overview of InSAR

SAR interferometry is a powerful and well-established remote sensing technique in which additional information from a scene is extracted from SAR complex images acquired by antennas at different positions or at different times. It was first demonstrated in 1974 by L.C. Graham (21), who obtained a pattern of nulls or interference fringes by vectorally adding the signals received from two airborne SAR antennas, one physically situated above the other.

The type of additional information that can be extracted with InSAR depends on the implementation of the system. If two SAR images are acquired from slightly different viewing geometries, information about the topography of the surface can be obtained. On the other hand, if the images are taken at slightly different times a map

of surface velocities can be produced. Finally, if sets of interferometric images are combined, subtle changes in the illuminated scene can be detected.

There are two basic implementations for SAR interferometry: single-pass or multi-pass.

- **Single-pass:** in single-pass SAR interferometry two antennas are mounted on an aircraft or a spacecraft in the same along-track position but displaced such that, seen from the target, one antenna is mounted above the other (Figure 2.24.a). Both antennas illuminate the same target area acquiring data simultaneously. With this configuration, the data needed for building the interferometric image is obtained in just one pass over the target area.

- **Multi-pass:** in multi-pass or repeat-pass SAR interferometry a single antenna is mounted on an aircraft or a spacecraft and the measurements are made in different passes over the target area (Figure 2.24.b). With this configuration, two passes over the target area are needed for building the interferometric image.

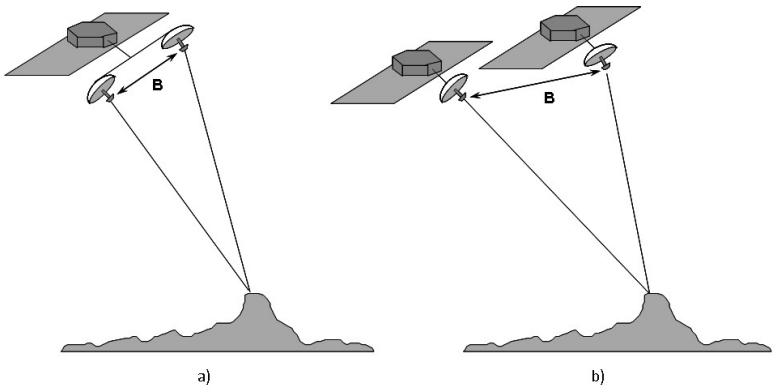

Figure 2.24: Single and repeat-pass interferometry. Schemes of single (a) and repeat pass interferometry (b). Image from (9).

There are two important concepts in SAR interferometry that must be presented: spatial baseline and temporal baseline.

- **Temporal baseline:** the temporal baseline is the time interval between two SAR acquisitions of the same area. In a pure temporal baseline situation a target area is imaged from exactly identical acquisition tracks at different times. The

fundamental principle is that with identical data acquisition situations the interferometric difference will be related to changes in the observed area. In single-pass configurations, the temporal baseline is determined by the distance between antennas and the speed of the moving platform and in multi-pass configurations the temporal baseline is determined by the time difference between passes over the target area.

- **Spatial baseline:** the spatial baseline is the distance between one acquisition track to the other (Figure 2.24). In a pure spatial baseline situation, the same target area is imaged from two different SAR tracks simultaneously (single-pass). The basic measurement is the estimate of the target height from the known platform positions and the ranges measured from the SAR antennas to the target. Thus spatial baseline provides terrain topographic information and allows the generation of DEMs.

2.4.2 Complex interferometric coherence

The complex interferometric coherence or simply the coherence between two complex SAR images s1 and s2 corresponds to the cross-correlation between them and is defined as

$$\gamma = E[s_1 \cdot s_2^*] \tag{2.24}$$

where *E[.]* means the expected value (that in practice will be approximated as a sampled average) and asterisk * denotes the complex conjugate. It is common to use the normalized version of this parameter that is

$$\gamma = \frac{E[s_1 \cdot s_2^*]}{\sqrt{E[|s_1^2|]E[|s_2^2|]}} \tag{2.25}$$

The modulus of the normalized complex interferometric coherence $|\gamma|$, commonly known as interferometric coherence, provides information about the quality of the interferogram and its value is between 0 and 1. In turn, the phase of the complex interferometric coherence or interferometric phase $\phi = \arg(\gamma)$ gives information about the path difference between the different antenna positions and the target.

Finally it is necessary to define two important concepts. On the one hand, an interferogram is defined as a 2D image where each pixel represents the interferometric

phase in each resolution cell of the imaged scene (Figure 2.25.b). On the other hand, the coherence map is defined as a 2D image whose pixels corresponds to the interferometric coherence value (modulus) of each resolution cell of the imaged scene (Figure 2.25.a).

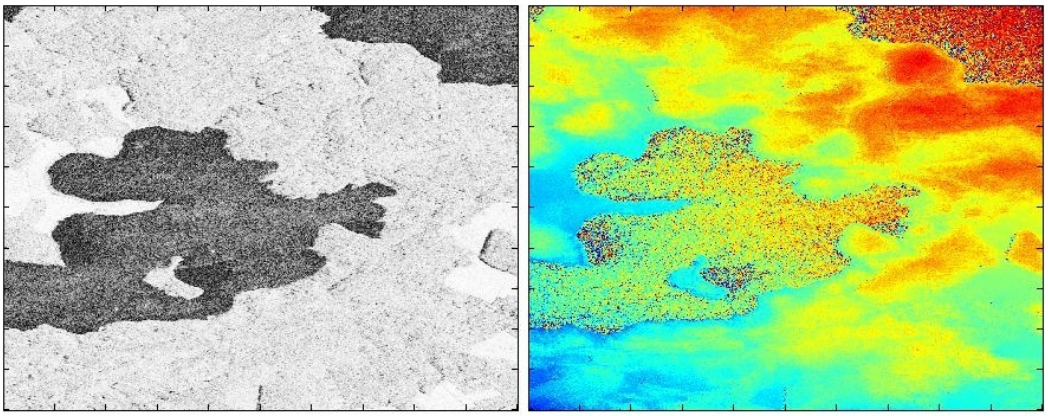

Figure 2.25: Coherence map and interferogram generated from two TanDEM-X SAR images over southern Finland. a)Coherence map. b) Interferogram.

2.4.3 Co-registration

Before generating the interferogram, a very accurate (sub-pixel) co-registration of the focused SAR images is required. The reason is that the different geometry of the SAR acquisitions generate translational shifts and rotational and scale differences between the images. In consequence, that incorrect alignment of the images reduces the coherence of the final interferogram and leads to inaccurate phase information. The process of aligning two (or more) SAR images of the same area acquired in the same mode is called co-registration. During this process, one of the SAR images is assigned as the master (reference) image and the other one as the slave (match) image. Through the whole co-registration process, only the slave image will be transformed. Generally, the co-registration process is performed in two steps: a coarse or rough registration and a fine or precise registration.

In the first step, coarse registration, the offsets are approximated either by defining common points in the image by visual inspection or by using track parameters. The considered transformations and re-sampling is applied to one of the images so that the

two images are registered at the pixel level. The co-registration accuracy at this step is usually up to one or two pixels.

In the second step, fine registration, the desired accuracy of the registration is on a sub-pixel level. Generally 1/10 pixel accuracy has become widely accepted for fine co-registration (25, 31, 59). Conventional techniques for precise co-registration are based on maximizing the cross correlation between the amplitude images (36, 37). The major drawbacks of these techniques are that, since co-registration is based only on the energy of the image rather than on its spatial structures, they are sensible to image geometry distortions (e.g. layover) and to noise. A second type of techniques tries to offer a solution to this problem by using the Fourier transform (FT) of the images (1, 61). With these techniques the spatial distribution of the structures in the image is taken into account since the spectral phase of an image preserves the location of the objects (47).

2.4.4 InSAR for measuring topography

The measurement of topography is one of the most important InSAR applications. The basic principles of height estimation can be explained using the geometry shown in Figure 2.26. Applying the law of cosines on the triangle formed by the two antennas and the point being imaged it follows that

$$(R + dR)^2 = R^2 + B^2 - 2BR\cos(\frac{\pi}{2} - \theta + \alpha) \tag{2.26}$$

where R is the slant range distance to the point being imaged from the reference antenna, dR is the path length difference between the two antennas, B is the physical interferometric baseline length, θ is the incident angle of the reference antenna to the point being imaged, and α is the baseline tilt angle with respect to the horizontal.

From Equation 2.26 and assuming that $R \gg B$ (common in most interferometers) the path length difference dR can be obtained as

$$dR \approx -B\sin(\theta - \alpha) \tag{2.27}$$

The SAR system does not measure directly the path length difference. Instead, what it is measured is an interferometric phase difference that is related to the path

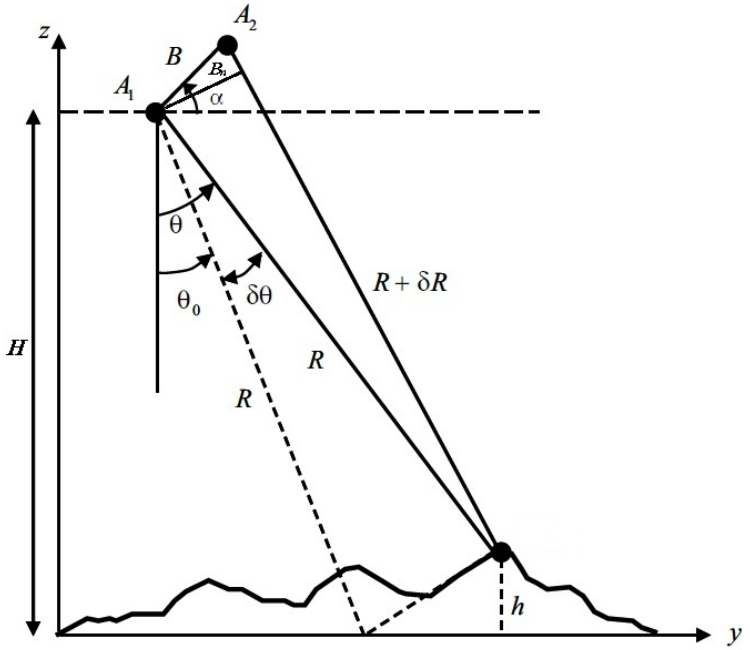

Figure 2.26: InSAR Geometry. Adapted from the image available at (9).

length difference through

$$\phi = \frac{a2\pi}{\lambda} dR = \frac{-a2\pi}{\lambda} B \sin(\theta - \alpha) \tag{2.28}$$

where $a = 1$ for the case in which signals are transmitted by one antenna and received through both at the same time (single-pass) and $a = 2$ for the case in which the signal is alternately transmitted and received through one of the two antennas only (multi-pass).

From Figure 2.26 it also follows that the elevation of the point being imaged is given by

$$h = H - R\cos(\theta) \tag{2.29}$$

with H denoting the height of the reference antenna above the reference plane with respect to which elevations are quoted (ground level).

Finally combining Equations 2.28 and 2.29 the elevation of the target point as function of measurable parameters and system parameters can be expressed as:

$$h = H - R\cos(\alpha - \arcsin(\frac{\lambda\phi}{a2\pi B})) \tag{2.30}$$

2.4.4.1 Interferogram flattening

The radar swath is not infinitely narrow, that is, it has a certain width. As a consequence the measured phase will vary across the antenna beamwidth causing the appearance of interferometric fringes parallel to the radar flight path even when imaging flat surfaces (Figure 2.27.a). In the case in which there is topographical relief in the imaged scene, those parallel lines are distorted by the presence of the relief as shown in Figure 2.27.b. Subtracting the smooth Earth interference pattern (Figure 2.27).a from the distorted pattern (Figure 2.27).b, the resulting interference pattern is known as the flattened interferogram and is shown in Figure 2.27.c.

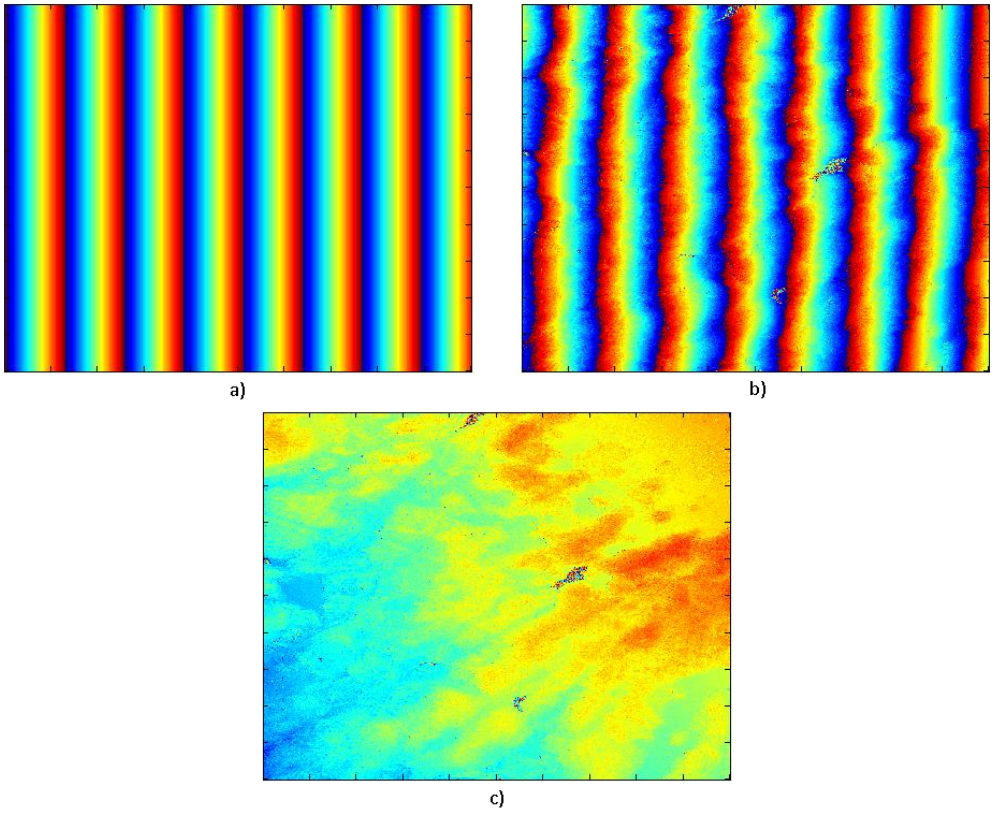

Figure 2.27: Topography of a scene expressed in form of the interferometric phase. a) Interferogram if there is no topography (smooth earth contribution). b) Actual interferogram (smooth earth + topography). c) Flattened Interferogram.

The presence of topography slightly modifies the incidence angle compared from the value in the absence of topography. From the geometry shown in Figure 2.26 it

follows that the change in the incidence angle introduced by the relief is

$$d\theta = \frac{h}{R\sin(\theta_0)} \tag{2.31}$$

where θ_0 is the incidence angle in the absence of relief for a given range.

From Equation 2.28 the phase of the pixel can be redefined as

$$\phi = \frac{a2\pi}{\lambda} B\sin(\theta_0 + d\theta - \alpha) \approx -\frac{a2\pi}{\lambda} B\sin(\theta_0 - \alpha) - \frac{a2\pi}{\lambda} B\cos(\theta_0 - \alpha)d\theta \tag{2.32}$$

The first term on the right in Equation 2.32 is the phase that would be measured in the absence of relief, that is, the phase shown in Figure 2.27.a. If this interferometric phase pattern due to a smooth Earth is subtracted from the actual interferometric phase, the resulting phase difference is the flattened interferogram. Combining Equation 2.28 and the second term of Equation 2.32, the flattened interferogram phase will be

$$\phi_{FLAT} = -\frac{a2\pi h}{\lambda R\sin(\theta_0)} B\cos(\theta_0 - \alpha) = -\frac{a2\pi B_n h}{\lambda R\sin(\theta_0)} \tag{2.33}$$

where $B_n = B\cos(\theta_0 - \alpha)$ is the baseline perpendicular to the line of sight. This equation describes the sensitivity of the radar interferometer to small height differences.

Defining the effective vertical (interferometric) wavenumber as

$$k_z = \frac{a2\pi B_n}{\lambda R\sin(\theta_0)} \tag{2.34}$$

the phase of the flattened interferogram will remain finally as

$$\phi_{flat} = k_z h \tag{2.35}$$

Notice that k_z depends only on the imaging geometry and the radar wavelength.

2.4.4.2 Phase unwrapping

The flattened interferogram provides an ambiguous measurement of the relative terrain altitude due to the 2π cyclic nature of the interferometric phase, in other words, the SAR system only measures phases between 0 and 2π (or between $-\pi$ and π, depending on the system). If the phase difference between two points reaches one of the lower

or upper limits there will be a phase jump in the recorded phase to keep the value between those two limits (Figure 2.28). Therefore, it is necessary to allocate this phase shifts and to correct them by adding or subtracting the correct number of cycles. This process is called phase unwrapping.

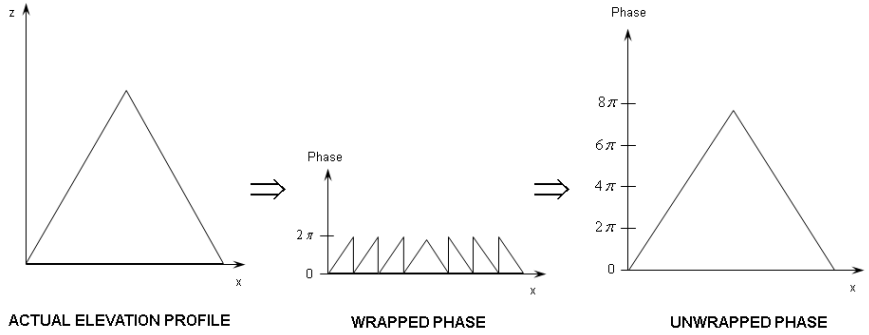

Figure 2.28: Phase unwrapping. Adapted from the image available at (8).

The earliest phase unwrapping routine was published by Goldstein et al. in 1988 (19). In this algorithm, areas in which the phase is discontinuous due to layover or poor signal-to-noise ratio are identified by cut-lines, and the phase unwrapping routine is implemented such those cut-lines are not crossed when unwrapping the phases. A second class of phase unwrapping algorithms are based on a least-squares fitting of the unwrapped solution to the gradients of the wrapped phase. This solution was first introduced by Ghiglia and Romero in 1989 (17). The major difference between these two classes of phase unwrapping algorithms lies in how errors are distributed in the image after phase unwrapping. Cut-lines algorithms localize errors in the sense that areas with low correlation are fenced off and the phase is not unwrapped in these areas, leaving holes in the resulting topographic map. In the case of least-squares algorithms, the unwrapping is the result of a global fit, resulting in unwrapping even in areas with low correlation. The errors, however, are no longer localized but instead are distributed through the image.

2.4.4.3 Absolute phase determination

Even after the phases have been unwrapped, the absolute phase is still not known and only differs from the absolute phase by an integer number of cycles. This absolute phase is required to produce a height map that is calibrated in the absolute sense,

in other words, to produce an actual height map. One way to estimate this absolute phase is to use ground control points with known elevations in the scene. However, this human intervention severely limits the ease with which interferometry can be used operationally. Madsen et al. reported in 1993 (42) a method by which the radar data itself is used to estimate this absolute phase. The method breaks the radar bandwidth up into upper and lower halves, and then uses the differential interferogram formed by subtracting the upper-half spectrum interferogram from the lower-half spectrum interferogram to form an equivalent low-frequency interferometer to estimate the absolute phase. Unfortunately, this algorithm is not robust enough in practice to fully automate interferometric processing.

2.4.4.4 Critical baseline

It becomes from Equation 2.33 that the best sensitivity to elevation is achieved by maximizing the electrical length of the interferometric baseline. In practice, however, it is not possible to arbitrarily increase this length. If the baseline becomes so large that the interferometric phase changes by more than 2π across one single pixel, the resulting interferogram will appear to have a random phase. The two main consequences of this are the occurrence of the speckle effect introduced in section 2.2.7 in the interferogram and the impossibility of unwrapping the phase to reconstruct the elevation profile. This situation will be even worse if the terrain slope is such that the surface is tilted toward the radar. The baseline length for which the two SAR images become completely decorrelated is known as the critical baseline B_{crit}. For flat surfaces, this can be expressed mathematically as (34, 57, 81)

$$B_{crit} = \frac{\lambda R \tan(\theta)}{r_{SR}} \tag{2.36}$$

where r_{SR} is the previously presented slant range resolution (section 2.2.3.4).

2.4.4.5 Problems of repeat-pass interferometry

There are two main problems that limit the usefulness of repeat-track interferometry. The first is due to the fact that the baseline of the repeat-track interferometer is not known accurately enough to obtain accurate elevation information from the interferogram.

The second problem is due to differences in scattering and propagation that result from the fact that the two images forming the interferogram are acquired at different times. The radar signal from each pixel is the coherent sum (i.e., amplitude and phase) of all the voltages from the individual scatterers contained in the radar pixel. If the individual scatterers in each pixel move between observations, the observed radar signal will change. The result is that the correlation between interferometric phases of neighboring pixels is lost, and the phase cannot be unwrapped reliably. This is known as temporal decorrelation, which is worst at the higher frequencies (81).

Moreover, in the case of spaceborne repeat-pass interferometry a further error source is atmospheric disturbances like variations of the tropospheric water vapor or ionospheric propagation delays, which lead to spatially correlated phase shifts in the final interferogram (24).

2.5 Polarimetric SAR Interferometry (Pol-InSAR)

Polarimetric SAR Interferometry refers to a combination of the explained techniques polarimetry and interferometry. Polarimetry allows to know the scattering properties of the target while interferometry provides information about the vertical structure of the target. Therefore, combining these techniques makes possible to separate different scattering centers distributed vertically. This technique enables the measurement of bio- and geophysical parameters of the Earth's surface such as topographical levels or vegetation heights.

Chapter 3

Material

Throughout this chapter the test site location, the instruments and the data sets utilized in this work are presented.

3.1 Test area

The area which serves as a test site for this thesis is located in southern Finland (60° 11' N, 24° 29' E), in the vicinity of Helsinki. It is a heterogeneous forest area which consists of small stands, alternating with fields and lakes. Forested areas are mostly located on the top of small hills. The dominant tree species are Scots pine, Norway spruce, birch, and alder. According to forest inventory information, the stem volume is up to 250 m^3/ha, with tree heights up to 30m. A 2012 satellite image from Google maps is shown in Figure 3.1.

3.2 Airborne E-SAR X-band interferometric images

The FINSAR campaign was carried out in autumn 2003 in Finland by the Laboratory of Space Technology, Helsinki University of Technology (TKK) (nowadays Department of Radio Science and Engineering, Aalto University) and the German Aerospace Center (Deutsches Zentrum fr Luft- und Raumfahrt; DLR). The test site was the described on section 3.1. and the main instruments used were a synthetic aperture radar E-SAR, operated by DLR, and a ranging scatterometer HUTSCAT, operated by TKK. The German E-SAR collected from 3km altitude five L-band (1.3GHz) repeat pass

Figure 3.1: 2012 Satellite image of the test area. Image from (20).

fully polarimetric images (5m, 10m, 12m and 0m baselines) and an X-band (9.6GHz) single-pass single-polarization (VV) interferometric image pair.

From the FINSAR campaign, only the data related to X-band measurements is used in this project. These files are the flattened interferogram, the vertical wavenumber and UTM geographical information and they are stored in binary format using 16 bits integers. In addition a text document with the all kind of acquisition information is also provided.

3.3 TanDEM-X mission

TanDEM-X (TerraSAR-X add-on for Digital Elevation Measurement) is an innovative spaceborne radar interferometer mission launched on June 2010 as an extension of the TerraSAR-X mission. In it the satellites TSX and TDX are orbiting together in a close formation at an altitude of about 500km, forming the first configurable SAR interferometer in space (Figure 3.2).

TanDEM-X mission is carried out by a public-private partnership between the German Federal Ministry of Education and Research (Bundesministerium fr Bildung und

Figure 3.2: TanDEM-X and TerraSAR-X flying in formation. Image from (15).

Forschung; BMBF), the DLR and Astrium GmbH. Its main objective is to generate an accurate three-dimensional image of Earth with homogeneous quality. The relevance of the mission lies in that, until now, the available DEMs of large parts of Earth are of low resolution, inconsistent, incomplete and commonly based on different data sources and survey methods. Now for the first time, a global, high accuracy and homogeneous DEM can be generated.

Besides the primary goal of the mission, several secondary mission objectives based on along-track interferometry as well as new techniques with bistatic SAR have been defined and represent an important and innovative part of the mission. (23)

3.3.1 TerraSAR-X

TSX is a German Earth-observation satellite launched on June 2007 that provides high-quality SAR images for scientific and commercial applications. Its primary payload is an advanced X-band radar satellite with a phased array antenna consisting of 384 transmit and receive modules. The antenna is fixed mounted to the spacecraft body and spans an overall aperture size of 4.8x0.7m. The center frequency of the radar instrument is 9.65GHz with a selectable range bandwidth of up to 300MHz. (64)

The configuration possibilities are numerous. Different imaging modes such as Stripmap (3m resolution, 30km swath width), ScanSAR (16m, 100km swath width), or Spotlight (1m, 10km image size) can be combined with different polarization settings. In addition, the TSX satellite has all the required features for the implementation of the TanDEM-X mission. Examples are additional X-band horn antennas for intersatellite phase synchronization, a dual-frequency GPS receiver for precise orbit determination and PRF synchronization based on GPS as a common time reference.

3.3.2 TanDEM-X

TDX is a rebuild of TSX with minor modifications like an additional cold gas propulsion system required for formation fine-tuning and an additional S-band receiver to enable the reception of status and GPS position information broadcasted by TSX (30).

3.3.3 Interferometric data acquisition

Interferometric data acquisition with the TanDEM-X satellite formation can be achieved in three different modes: bistatic, monostatic, and alternating bistatic (Figure 3.3). The three interferometric modes can be further combined with the already mentioned imaging modes (Stripmap, ScanSAR and Spotlight). The data received from DLR for this project was acquired using stripmap and bistatic mode.

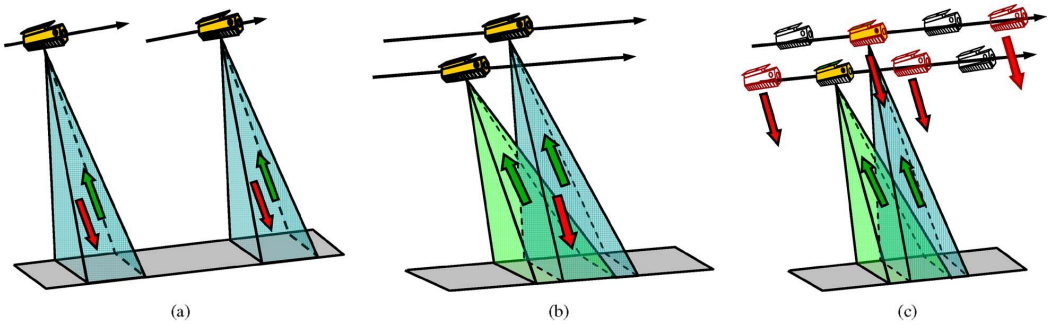

Figure 3.3: Data acquisition modes of TanDEM-X. a) Pursuit monostatic mode. b) Bistatic mode. c) alternating bistatic mode. Image from (30).

In the bistatic mode (Figure 3.3.b) either TSX or TDX illuminates the Earth's surface and both receive and record the scattered signal simultaneously. This simultaneous data acquisition makes possible to avoid errors due to temporal decorrelation and atmospheric disturbances. An essential requirement for radar interferometry is

a sufficient overlap of the two recorded Doppler spectra. In bistatic mode, the two Doppler spectra are mutually shifted, and the amount of this shift is linearly related to the along-track displacement between TSX and TDX. The maximum along-track separation in bistatic stripmap mode should always stay below 1 km to ensure a sufficient overlap of the Doppler spectra. In addition, PRF synchronization and relative phase referencing between the two satellites are mandatory in the bistatic DEM generation mode. (30)

3.3.4 TanDEM-X data set

The data set received from DLR is constituted of 8 experimental products with single-pass multi-polarization (HH and VV) measurements carried out between August 2011 and January 2012 over the test site. Each of these products consists of two level 1b products (one from TSX and the other one from TDX), WGS-84 geographical information, acquisition information, preview images and some other files that lack of interest for this project.

Each level 1b product include a co-registered single look slant range complex (CoSSCs) image data file which is packed using the COmplex SAR (COSAR) file format. At the same time, each COSAR file contains all focused complex SAR data of one beam in a burst by burst order together with sample validity and position annotation. In the case of this project the received products are stripmap images which consist only of one burst. The complex SAR data samples are stored as 16bit/16bit complex floating point numbers (IEEE norm 754-2008) in the same order as they are recorded by the SAR instrument (near range sample first). The byte order is big-endian (most significant byte (MSB) first). All annotation and filler values are stored as 32 bit integer (4 bytes). In Figure 3.4 a scheme of the data structure is shown. (13)

3.4 Light Detection And Ranging (LIDAR) measurements

In addition to E-SAR and TanDEM-X data, LIDAR measurements of the canopy height and terrain elevation over part of the FINSAR test site (Figure 3.5) are also used as reference and auxiliary data. The laser scanning was performed by the Finnish Geodetic Institute on July 2005 using a laser scanner Optech ALTM 3100 unit with 100kHz PRF at 1km flight altitude. This provided a target point density of 3-4 pts/m^2. The

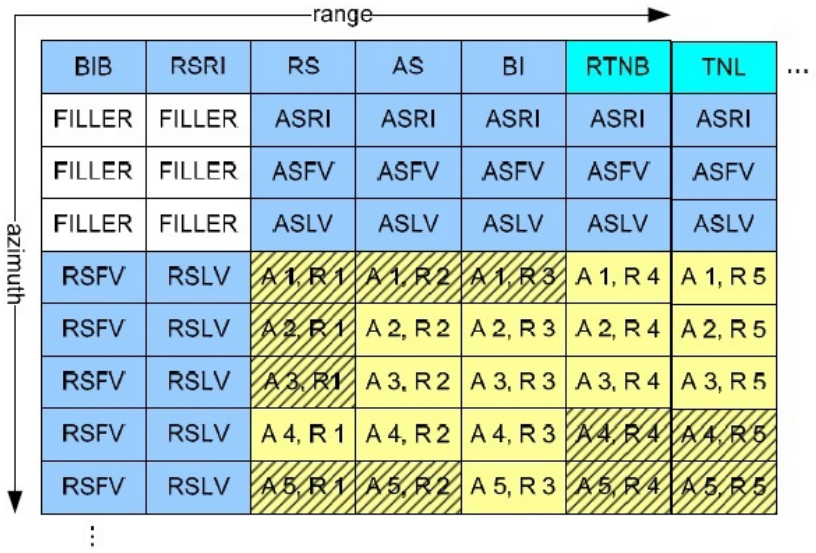

Figure 3.4: TanDEM-X COSAR file structure. Image from (13).

strip adjustment (matching adjacent flight strip data) was produced using TerraMatch software. Ground hits were classified using TerraScan (2). A digital surface model (DSM) relevant to treetops was obtained by taking the highest point within a 1m grid, with missing points interpolated by Delaunay triangulation. The Canopy Height Model (CHM) (Figure 3.5.b) was obtained by simply subtracting the ground DEM (Figure 3.5.a) from the corresponding treetop DSM. The crown DSM was calculated by means of the first pulse echo while the DEM used the last pulse echo.

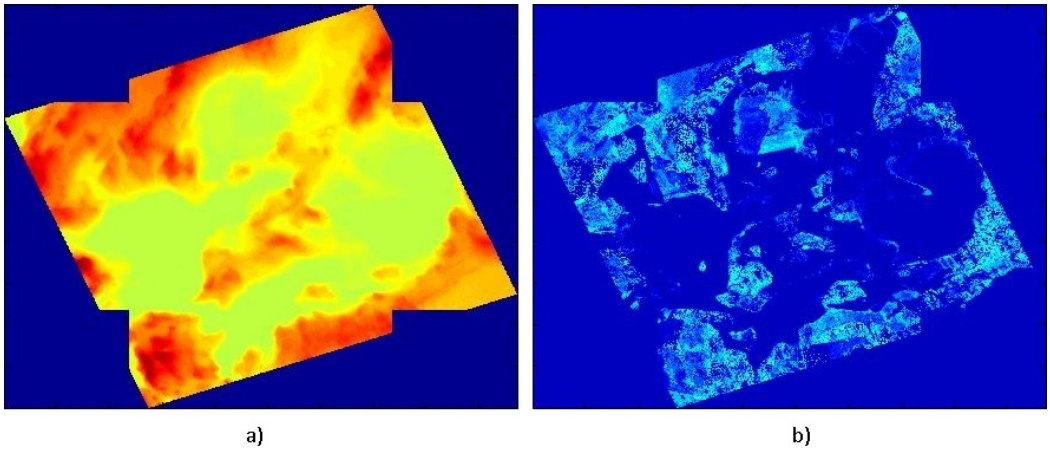

Figure 3.5: DEM and CHM of the test area. a) DEM. b) CHM.

The accuracy of the obtained DEM was noted to be better than 20 cm for forested terrain. The CHM had a -70 cm bias in the obtained tree heights and an root mean square error of 0.5m. This means that LIDAR measurements are highly precise but it is important to remark that they are very expensive to carry out and they cannot be made above cloud cover or when fog, smoke, rain, or snow storms are present. The data is geocoded using the UTM system.

Chapter 4

Methods

In this chapter all the processing steps that have been applied to the project data are presented. First an overview will be given and after that the details of every step will be explained. The main work environment and programming language used has been MATLAB although a Java applet has been also developed.

4.1 Processing overview

The goal of this thesis is to compare the height information that can be extracted from two different X-band SAR data sets, E-SAR and TanDEM-X, using LIDAR measurements as high precision auxiliary reference data. Although three different data sets are used, most of the effort in current thesis has been on preprocessing the recent TanDEM-X mission data.

In order to accomplish the objective of the work two interferograms have to be generated, one from E-SAR data and another from TanDEM-X data. The phase of these interferograms represents height variations in the phase domain, that is, with values ranging between $-\pi$ and π. In order to have actual height variations, the vertical wavenumber for each data set must be calculated and Equation 2.35 applied. After converting the scattering center height to metric height, a comparison with DEM and CHM can be made. In order to compare the three data sets, E-SAR and TanDEM-X data must be converted from slant range to a common coordinate system. The UTM geographic coordinate system is used in this work as a common 2D coordinate system for the data comparison as the laser data is already provided in this system. Using the

geographical information available it is possible to ascertain the portion of terrain common to the three data sets and everything can be converted and represented together in geographical coordinates. An scheme of the whole processing chain is presented in Figure 4.1.

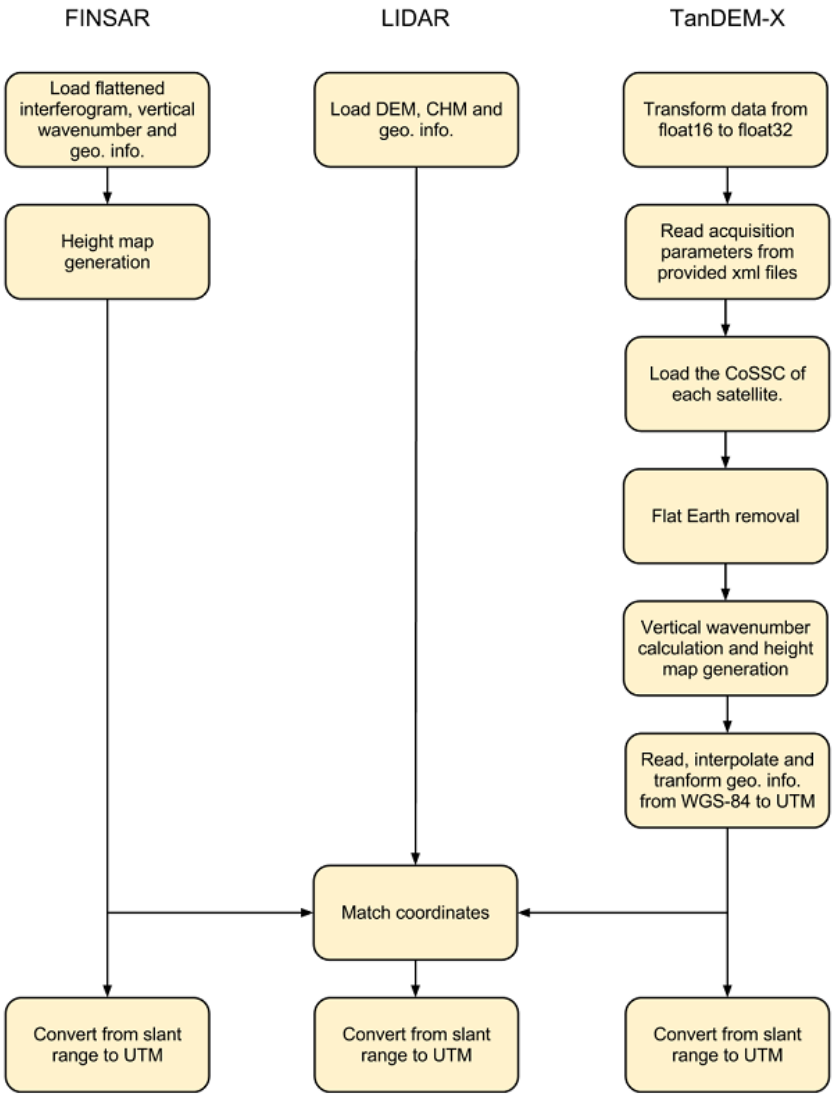

Figure 4.1: Processing steps for TanDEM-X, E-SAR and LIDAR data.

4.2 E-SAR data processing

The required processing of E-SAR X-band data set is rather straightforward since DLR provided interferograms in both slant and ground range in geographical coordinates system. The processing steps of co-registration, interferogram generation and flattening and vertical wavenumber calculation were already performed and the results were stored in the supplied binary files.

The first task to carry out is reading into memory the flattened interferogram and the vertical wavenumber files. This is done by using a MATLAB script that was developed by members of the Radio Science and Engineering department of Aalto University during earlier studies. This script uses MATLAB internal functions such as *fread()* or *fseek()* to load a desired portion of the files. In this case the desired part is the one containing the area under study.

Once the data is loaded, the next step consists of converting the phase variations of the interferogram to actual height variations. This is achieved by applying Equation 2.35 to the flattened interferogram and the vertical wavenumber data.

4.3 Laser data processing

Laser measurement processing was carried out by Finnish Geodetic Institute. Digital Elevation Model and Canopy Height Model were provided in UTM coordinates. The provided binary files are loaded into memory using MATLAB functions. As the laser measurements were performed just in a small area, DEM and CHM files are small and fit easily into memory. The geographical UTM information consisting in the corner coordinates and the pixel spacing in northing and easting directions can be also read from those files.

4.4 TerraSAR-X and TanDEM-X data processing

The understanding and processing of the TanDEM-X mission data has been the main work carried out for this thesis. This section describes all the steps performed in order to obtain a height profile of the test site from the received TSX and TDX CoSSCs products.

4.4.1 Transformation of data from float16 to float32

The latest TSX and TDX CoSSCs use 2-byte precision floating point numbers for storing complex samples. This format is not widely supported by the main programming languages including C, Java or even MATLAB. Furthermore, this data format has begun to be used by DLR in its data recently so the main free remote sensing tools as ESA's NEST does not support it yet. Considering this, the first task to carry out is to convert the data to a more common data format. The regarded options were 2-byte integers or 4-byte floating point numbers. Although the required disk space is bigger, in order to avoid the loss of precision the chosen option was the so called single precision floating point format (4 bytes). Following the IEEE-754-2008 norm and the data structure specifications provided by DLR (briefly presented in section 3.3.4) a JAVA applet is implemented in order to accomplish this transformation. Basically the developed program takes as an input the COSAR file, reads the headers and the invalid sample markers, reads the 16-bit floating point values, transforms them to 32-bit floating points numbers and creates as an output a binary file containing just the complex samples in single precision format and the size information stored as 32-bit integers. In Figure 4.2 a capture of the simple interface of the program is shown and in Figure 4.3 the output files of the program are represented.

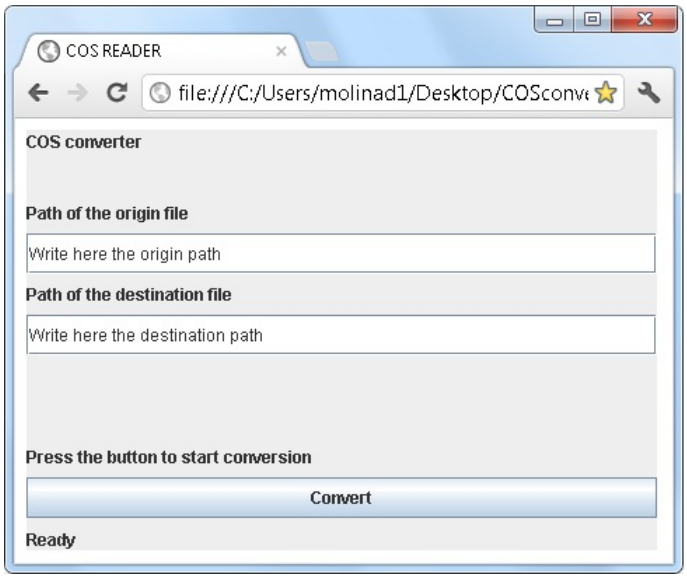

Figure 4.2: Interface of the applet that transforms the half precision float COSAR files to single precision binary files.

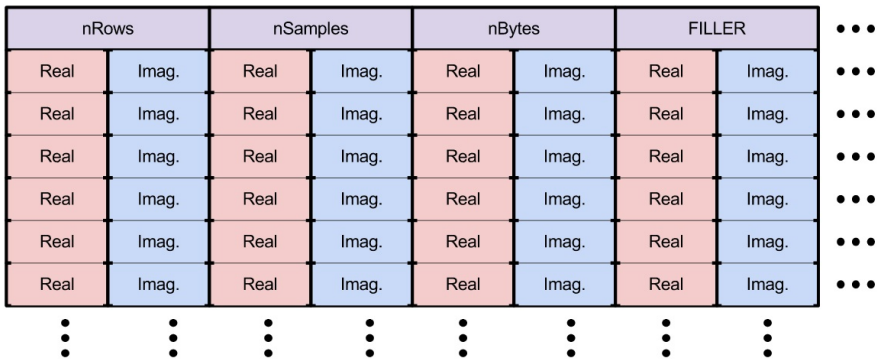

Figure 4.3: Structure of the output files of the Java Applet.

4.4.2 Loading the data into MATLAB

The next step is loading the data into MATLAB. Considering that the SAR images are too big to handle them as a single piece, just the area of interest of the image is loaded into memory and processed. The implemented function receives as input the interval of rows and columns that is going to be read. It is important to note that, as the satellites store the samples as they record them, the direct representation of the data is different depending if the acquisition was made in an ascending or a descending pass of the satellite (Figure 4.4). In ascending pass images the direct representation of the data looks like the provided previews and the actual map. However, in descending pass data the image look rotated. In order to avoid confusions when selecting the part of the image to read, internally the function transforms the received indexes when the orbit direction is descending and rotates the image so that everything looks like in the previews or in the map. The information about the orbit direction is read by another MATLAB function from the also provided information xml file.

Finally, for post-processing steps it is very important to know clearly at this point where in the image is the origin of range and azimuth as for descending pass the image has been rotated 180°. In ascending passes it is located in the lower left corner (Figure 4.5.a) and in descending passes it is located in the upper left corner of the image (Figure 4.5.b).

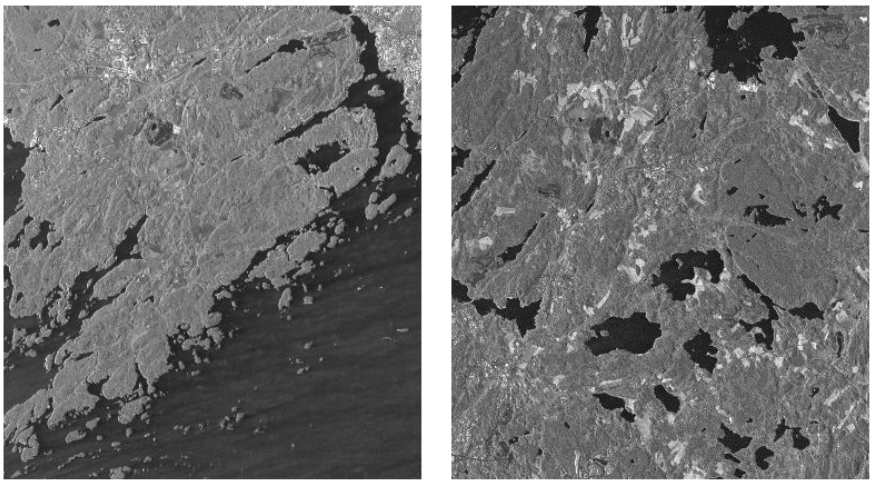

Figure 4.4: Direct representation of two COSAR files. a) acquired during an ascending pass. b) acquired during a descending pass.

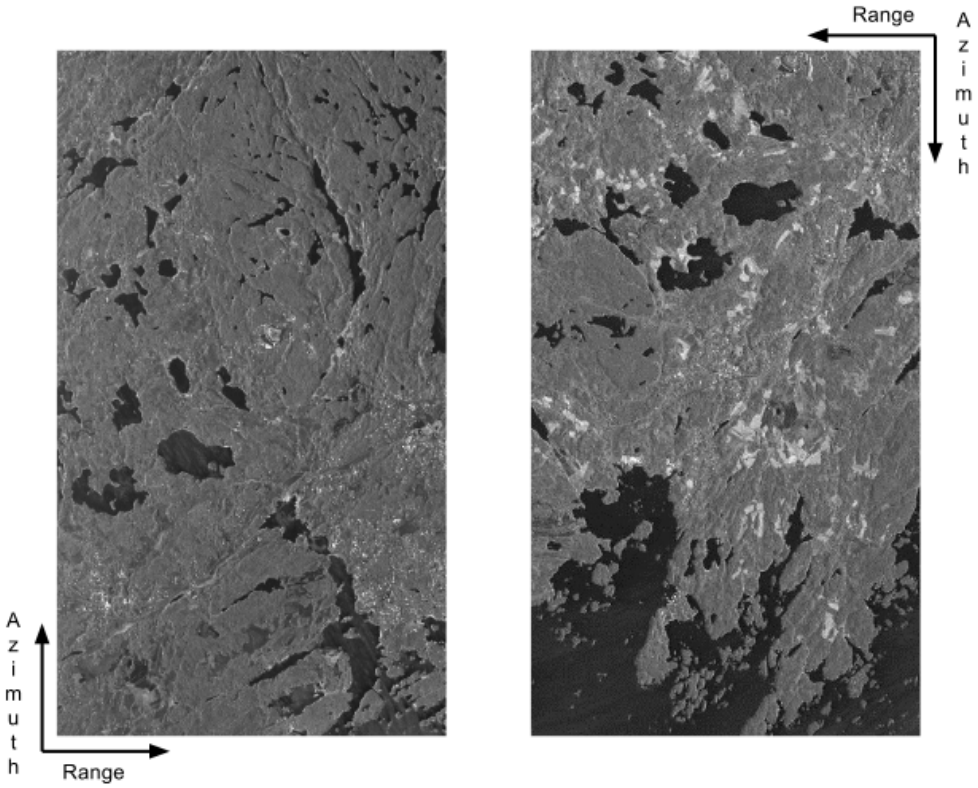

Figure 4.5: SAR image reference axis. a) Acquired during an ascending pass. b) Acquired during a descending pass.

4.4.3 Interferogram generation

Once it is possible to read correctly the data, the interferogram of the test site is generated. To do this, first a suitable experimental product is selected and the part of the image containing the area of interest is loaded from each satellite COSAR file. The selected product was acquired using VV polarization which is the same scheme used in E-SAR data. The interferogram is generated by calculating the normalized complex interferometric coherence (Equation 2.25) between the two images. As the last step, the interferogram is filtered with a smoothing 2D (5x5) FIR filter in order to reduce the noise and speckle. The interferometric coherence and phase of the resulting image are shown in Figure 4.6.

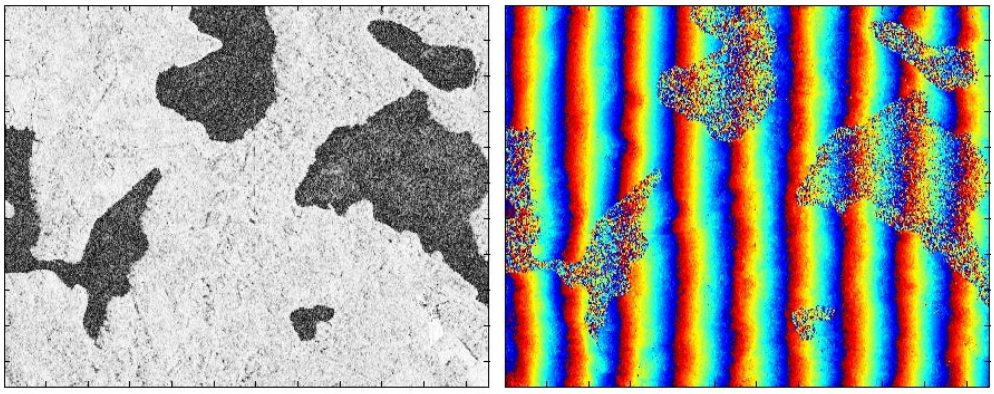

Figure 4.6: Interferometric coherence and phase of the test site. a) Interferometric coherence. b) Interferometric phase.

4.4.4 Flat earth phase calculation and interferogram flattening

It becomes obvious from Figure 4.5.b that the interferometric phase is subjected to the flat earth effect described in section 2.4.5.1. For obtaining valid height information from the interferometric phase it is necessary to firstly remove this effect by calculating the phase component due to flat earth and subtracting it from the interferogram. This phase component can be easily calculated applying the formula introduced in (63) and defined like

$$\phi_{flate} = \frac{2kB_{eff}dR}{R_0 \tan(\theta_0)} \tag{4.1}$$

to each resolution cell (pixel) of the image. In this equation k is the wavenumber, R_0 the range distance to the nearest resolution cell, dR the difference between R_0 and the range distance of the resolution cell under consideration, θ_0 the look angle to the nearest pixel and B_{eff} the perpendicular or effective baseline.

The required parameters can be directly read or calculated from image parameters provided in the xml files together with the data. The look angle and the effective baseline are read directly from the file. The wavenumber can be calculated reading the central frequency of the radar from the file and applying Equation 2.5. Finally, for calculating the range distances from each pixel to the radar it is necessary to interpolate since the range times for only the first and last pixel of the image are given. First the time values are converted to distance values by simply applying

$$R = \frac{tc_0}{2} \tag{4.2}$$

Knowing those two distance values and the number of pixels in a range line it is simple to apply linear interpolation and obtain the values of the flat Earth phase for the whole image (Figure 4.7.a). When subtracting the flat earth pattern from the distorted interferogram (Figure 4.6.b) the flattened interferogram is obtained (Figure 4.7.b).

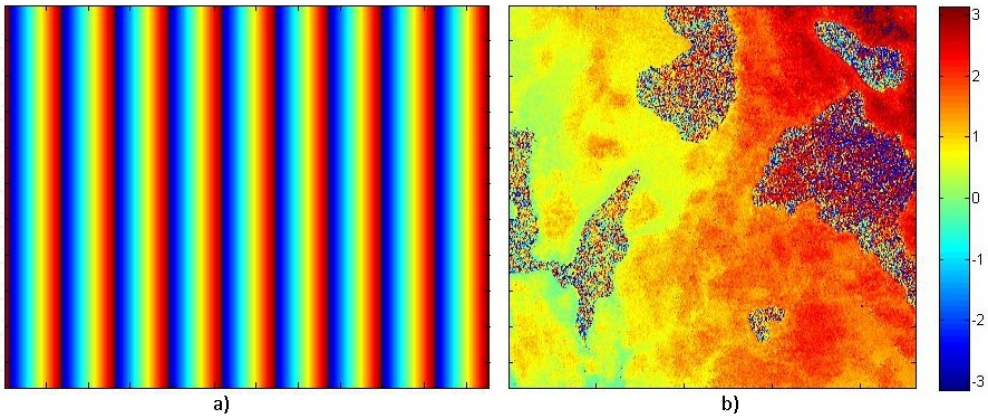

Figure 4.7: Flat Earth phase pattern for the test image and flattened interferogram. a) Earth pattern. b) Flattened interferogram. Scale is in radians.

4.4.5 Vertical wavenumber calculation

At this point the height variations at the study area are represented in the phase domain, that is, the values range between $-\pi$ and π. For going from phase variations to

actual height variations it is necessary to calculate the vertical wavenumber (Equation 2.34) introduced in section 2.4.5.1. All the needed parameters are obtained in the previous stage except the look angle for each resolution cell. The procedure to obtain this parameter is identical to the one for obtaining the range distances for the flat earth pattern calculation, but now the values read from the xml file are the incidence angle at the first and the last pixel of the image. The vertical wavenumber pattern of the test image is shown in Figure 4.8.a and the result of transforming the flattened interferogram from phase variations to actual height variations can be seen in Figure 4.8.b.

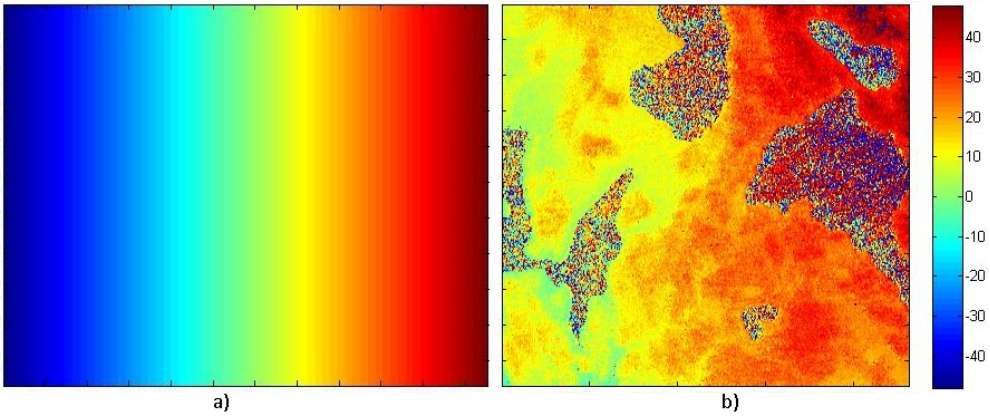

Figure 4.8: Vertical wavenumber and real height variations at the study area. a) Vertical wavenumber. b) Real height variations (m).

4.4.6 Geolocating the images

The next step is to assign every SAR pixel with the correct coordinate on the ground. The geolocation information for TanDEM-X images is given for just some pixels of the image. The geodetic system WGS-84 is used (Figure 4.9). In order to use a regularly spaced pixel grid, WGS-84 coordinates are projected to the UTM system utilizing a public MATLAB function available at (48).

In order to have values for all the pixels in the image, the geolocation grid is interpolated using the MATLAB function *interp2()*.

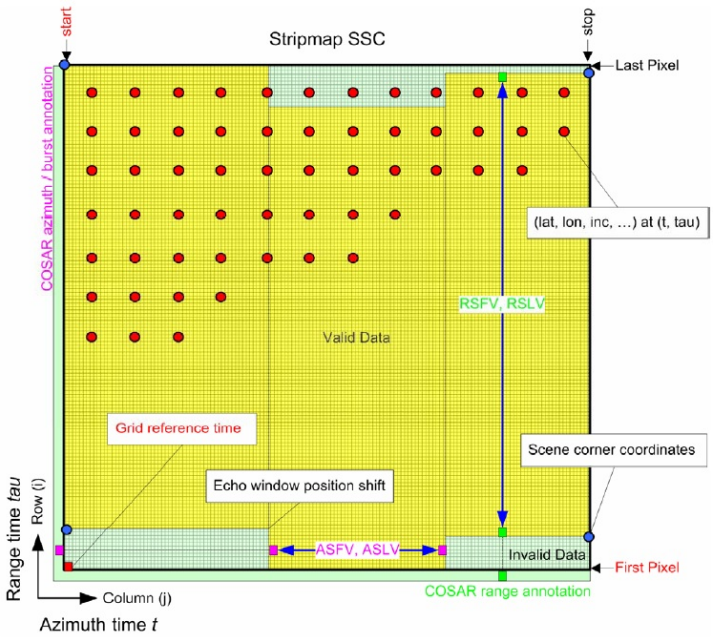

Figure 4.9: Geolocation grid, scene coordinates and COSAR image raster for CoSSCs. Image from (13).

4.5 Area selection and image conversion

SAR data is ready to be transformed and represented together in geographical coordinates but first it is necessary to select the part of the study area for which data from E-SAR, LIDAR and TanDEM-X is available. Since the UTM coordinates of the three images are known, it is straightforward to select the range of coordinates that match in the three images. The pixel spacing in the resulting images is $2m$.

The area of interest on E-SAR data and TDX is transformed to the UTM system. In the case of E-SAR this is done by using two conversion tables that were provided together with the SAR data. Each table is represented in UTM coordinates and each cell of the table has an index value. In one table these indexes correspond to range values on the SAR image and in the other to azimuth values. For carrying out the transformation, first the part of the tables corresponding to the desired area is selected and then, consulting the range and azimuth indexes, a new image is filled with the corresponding values of the SAR image. This process is shown in Figure 4.10 and the result in Figure 4.11.

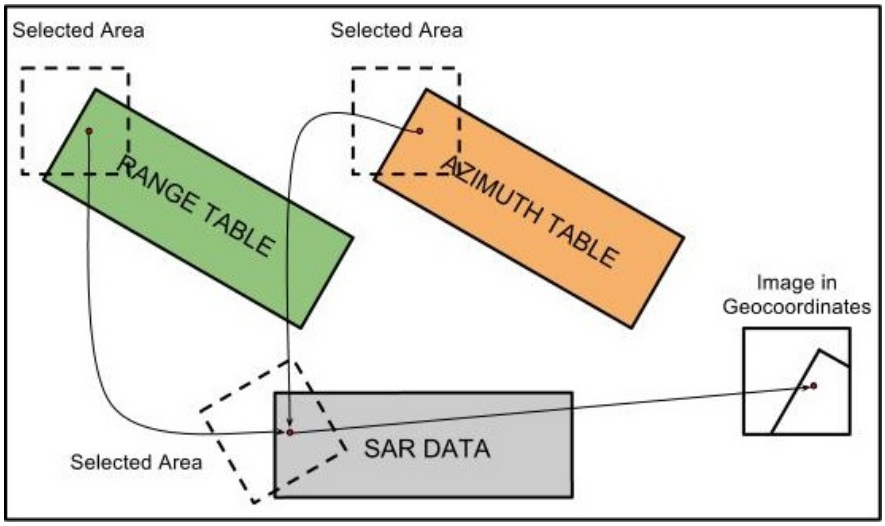

Figure 4.10: Procedure for transforming slant range E-SAR data into geographical coordinates.

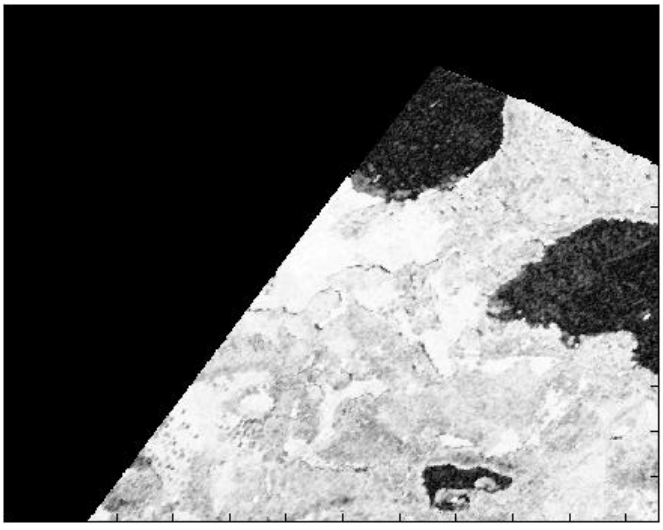

Figure 4.11: E-SAR coherence image of the study area in geographical coordinates.

TanDEM-X data is transformed from slant range geometry to UTM by using the coordinate values for each pixel previously obtained. The procedure is directly to read the coordinates of each pixel and to place it in the right place in the resulting image. The result is shown in Figure 4.12.a and as it can be appreciated there are holes in the image because of the change of geometry. For visual purposes only the image holes can be filled by interpolation (Figure 4.12.b). It is important to remember that the phase information of interpolated pixels is not really measured and therefore it should not be used in the analysis. However, visual inspection of the images is much easier when the gaps in the image are filled up.

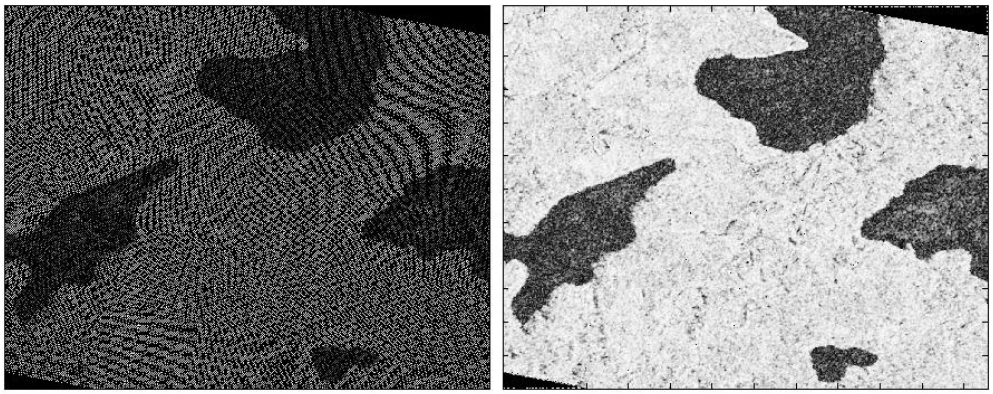

Figure 4.12: TanDEM-X coherence image of the study area in geographical coordinates with and without interpolating the non existing values. a) Coherence image in geographical coordinates. b) The same image interpolating the non existing values.

Laser data is already in geographical coordinates so selecting the appropriate part of the image is enough (Figure 4.13).

For checking that all three data sets are correctly geocoded to UTM, a RGB composite image is created with E-SAR data in the red channel, CHM in the green channel and TDX data in the blue channel (Figure 4.14).

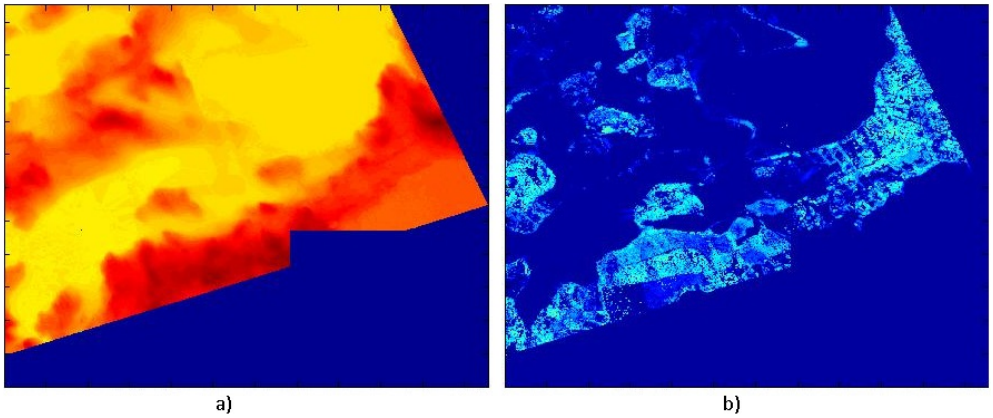

Figure 4.13: Selected part of DEM and CHM. a) DEM. b) CHM.

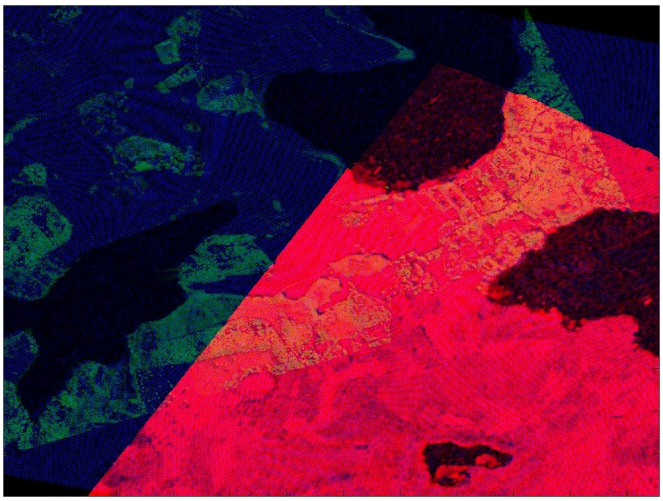

Figure 4.14: Composite RGB image of the test area with E-SAR data in the red channel, CHM in the green channel and TDX data in the blue channel.

Chapter 5

Results and discussion

In this chapter are presented the main results of this work. The tree height estimation comparison between TanDEM-X, E-SAR and LIDAR data is given by means of different figures, graphics and numerical results. Moreover, the ability of TanDEM-X to produce reliable canopy height information is analyzed and discussed.

5.1 Coherence analysis

In this section, coherence images generated from TanDEM-X and E-SAR data are compared with each other and with the canopy height model. As it can be appreciated in Figure 5.1, in the E-SAR image it is possible to distinguish between lakes, open areas and forest areas more clearly than in the TanDEM-X coherence magnitude image. Lakes present very low coherence and appear as black areas due to the very low backscattered signal level caused by the specular reflection of the transmitted signals. Open areas appear as bright areas due to the high coherence caused by the direct backscatter of the transmitted signals. Forests appear gray and show some dynamics in brightness because they present random variations in the coherence values due to the volume decorrelation. Since TanDEM-X data has been acquired from a $514km$ space orbit, it presents a smaller signal to noise ratio than E-SAR data. Probably, that makes coherence values more similar and therefore the distinction between open and forest areas is more difficult. These smaller dynamics of coherence values in TanDEM-X images can be also caused by the different imaging conditions. As in this work only

one TanDEM-X interferometric pair is used, the dynamics of coherence amplitude and its causes are not further analysed.

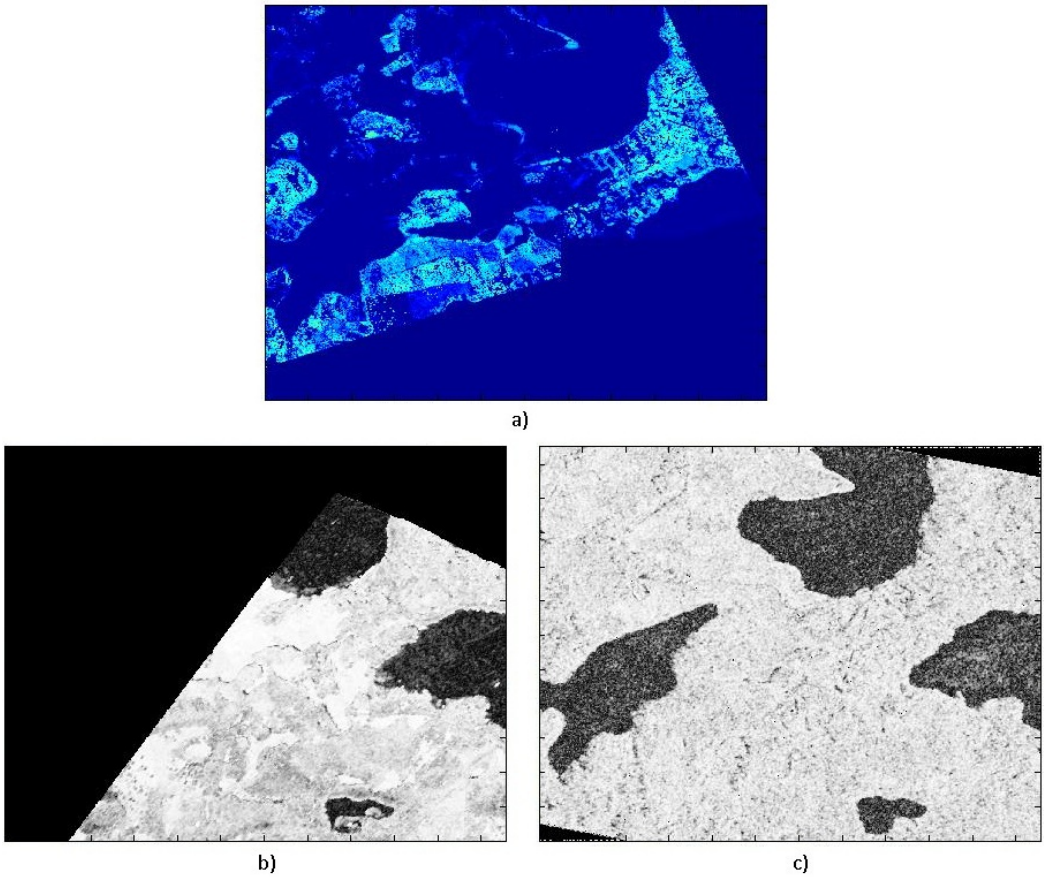

Figure 5.1: CHM and coherence images from E-SAR and TanDEM-X at the test area. a)CHM. b) E-SAR coherence. c) TanDEM-X coherence.

5.2 Interferometric phase center location

In this section, the interferometric phase and thus the elevation information in the interferometric images is reviewed. In Figure 5.2 are shown the elevation maps generated from E-SAR (Figure 5.2.b) and TanDEM-X (Figure 5.2.c) data together with the LIDAR generated DEM (Figure 5.2.a) of the area. When comparing the images it can be observed that both interferograms give roughly similar estimation of the height tendencies at the test area which compare well with the reference data. Notice that

the color scales of the interferometric images are somewhat different because interferometry does not give absolute values of the elevation. An small exception is found on E-SAR image (b), where near range part of the image (upper right part of the image) is depressed. This effect is compensated in the later comparison.

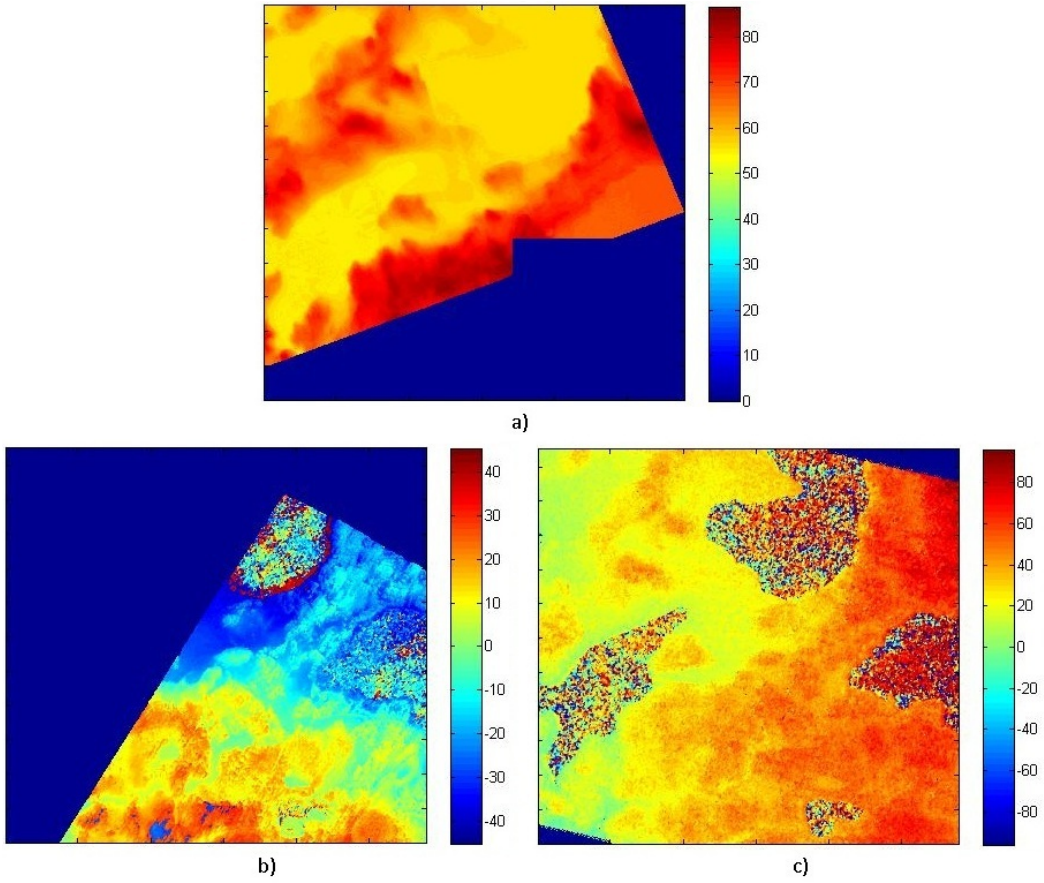

Figure 5.2: DEM and height variation images from E-SAR and TanDEM-X at the test area. a) DEM. b) E-SAR height variation image. c) TanDEM-X height variation image. Scales are in meters.

In order to study the height variations in more detail, two different transect lines are taken from each of the 3 images (TanDEM-X, E-SAR and DEM) and represented in 2D plots were the y-axis represents the height and the x-axis represents the distance on the ground. In Figures 5.3.a and 5.4.a are represented together a profile views of the DEM (blue line) and the canopy height model (green line). In Figures 5.3.b and 5.4.b the scattering phase elevation extracted from the E-SAR image is represented and as

it can be appreciated the height tendency is followed very well. As it can be seen, the SAR reflection seemingly comes from inside of the forest canopy or from the surface of the ground. In (52) it was demonstrated that the interferometric scattering phase center is located close to the 75% of the real height in forest areas. In Figures 5.3.c and 5.4.c the height variations extracted from TanDEM-X data are represented. It can be observed that the phase center elevation line is much noisier than with E-SAR data. This is probably because spaceborne SAR requires a very precise measurement of the orbit and the acquisition parameters as well as of the received signal. Any small error becomes significant due to the great distance to the target. The signal to noise ratio of E-SAR airborne measurement appears to be much better that the signal to noise ratio of the TandDEM-X measurement.

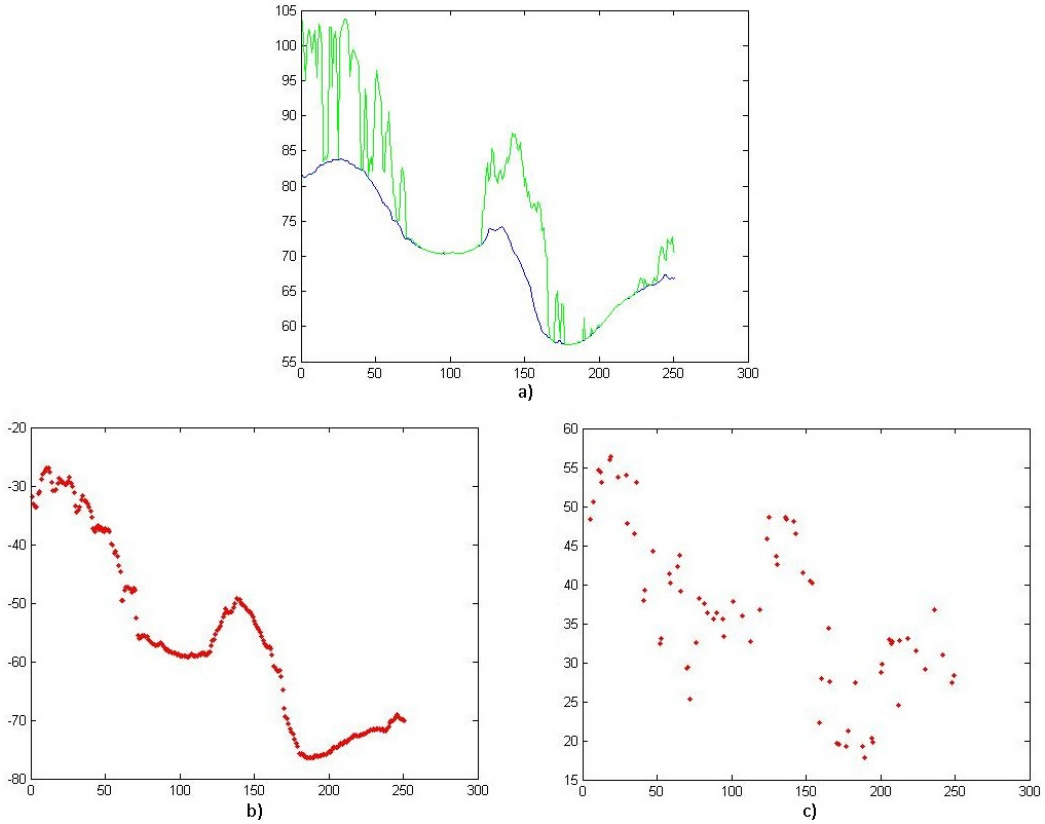

Figure 5.3: Height variations at the same transect track of the study area. a) DEM (blue line) and CHM (green line). b) E-SAR data. c) TanDEM-X data. The y-axis represents actual height (m) in plot a) and height variations (m) in plots b) and c). The x-axis represent the relative distance (m) on the ground.

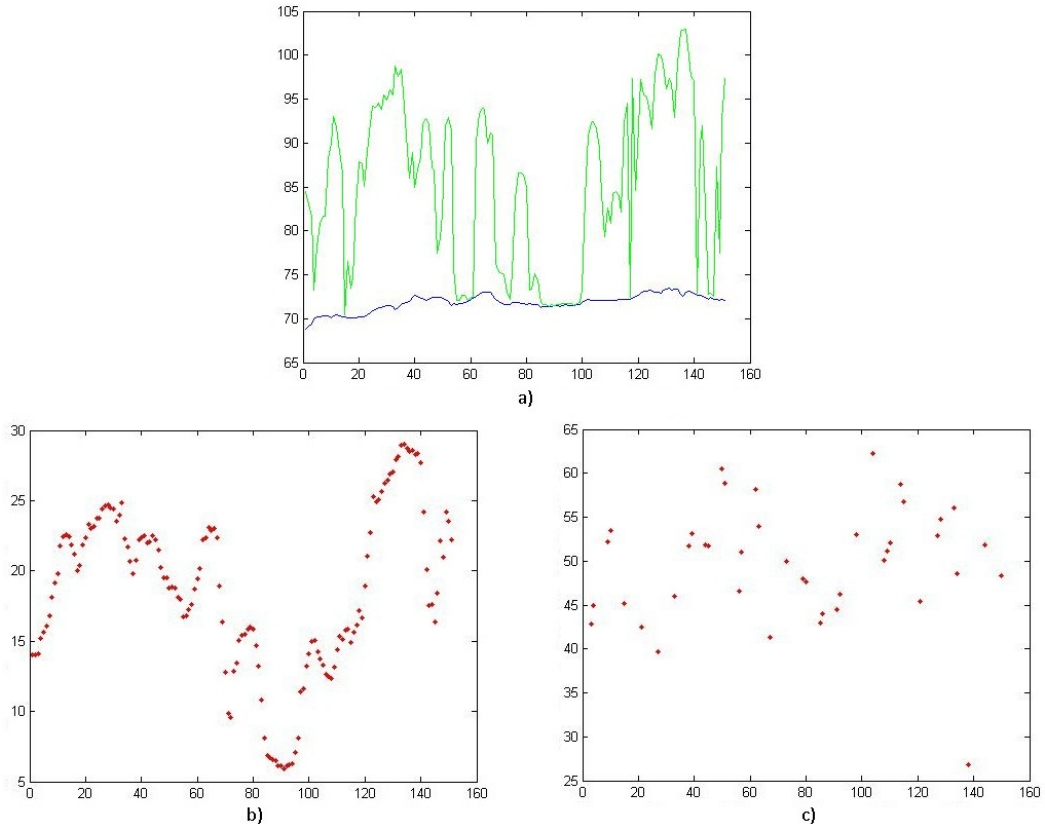

Figure 5.4: Height variations at a second transect track of the study area. a) DEM (blue line) and CHM (green line). b) E-SAR data. c) TanDEM-X data. The y-axis represents actual height (m) in plot a) and height variations (m) in plots b) and c). The x-axis represent the relative distance (m) on the ground.

In order to obtain a quantitative measurement of the height estimation accuracy that can be achieved with each of the used SAR data sets, the correlation between phase center height and LIDAR measured elevation model is calculated. This was made separately for forested areas and open areas. For open areas, SAR reflection comes from the ground, and high correlation between elevation of SAR reflection and the accurate ground elevation model can be expected. However, for forested areas the scattering center locates inside the forest layer and correlation should be lower. Additionally to this effect, it has to be taken into account that tree height model measured by LIDAR was acquired several years before TandDEM-X measurements and some parts of the forest may have changed significantly. Correlation analysis results are presented in Table (Table 5.1). The 4 plots representing the scattering between LIDAR and estimated height for E-SAR and TanDEM-X data and for ground and forest areas are shown (Figures 5.5 - 5.8). In the case of E-SAR data, the DEM has been shifted to the same range than the SAR data by using a fitting algorithm implemented in (52) that also corrects the previously mentioned depression problem.

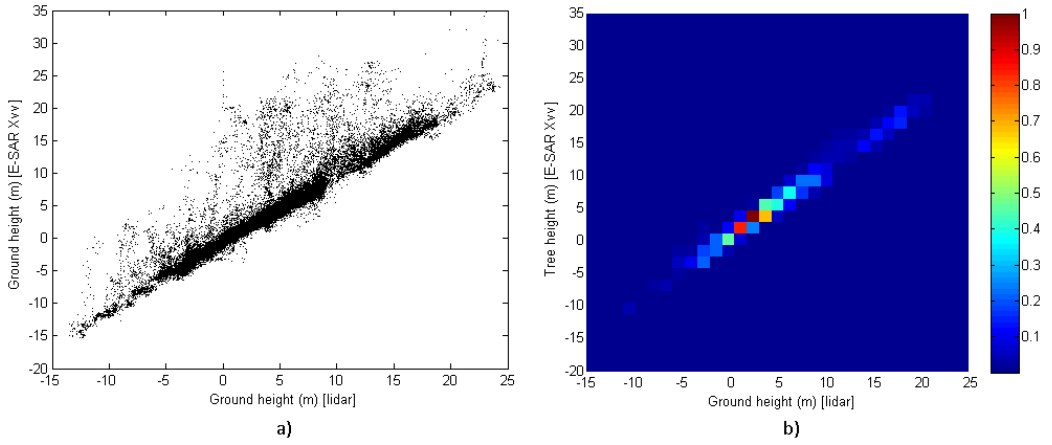

Figure 5.5: Relationship between E-SAR X-band interferometric height variations (m) using VV polarization (y-axis) and LIDAR height measurements (m) in ground areas (x-axis). a) Scatter plot representing this relationship. b) 2D histogram representing this relationship. Colors indicates the amount of samples in each bin normalized by maximum amount of samples in one bin.

As it can be observed in Figure 5.5 and 5.6 and in Table 5.1, E-SAR data has high correlation with the DEM, especially in non-forested areas. This indicates that in open areas SAR reflection really comes from the ground and interferometric processing

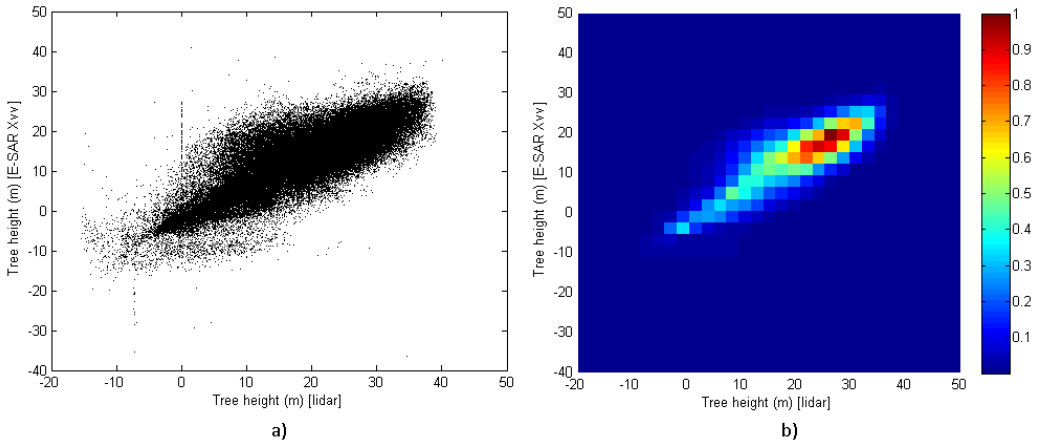

Figure 5.6: Relationship between E-SAR X-band interferometric height variations (m) using VV polarization (y-axis) and LIDAR height measurements (m) in forest areas (x-axis). a) Scatter plot representing this relationship. b) 2D histogram representing this relationship. Colors indicates the amount of samples in each bin normalized by maximum amount of samples in one bin.

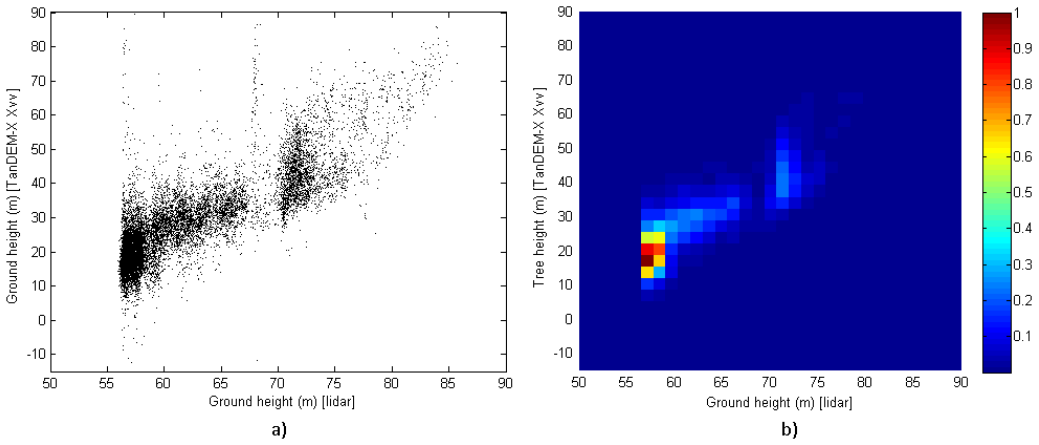

Figure 5.7: Relationship between TanDEM-X X-band interferometric height variations (m) using VV polarization (y-axis) and LIDAR height measurements (m) in ground areas (x-axis). a) Scatter plot representing this relationship. b) 2D histogram representing this relationship. Colors indicates the amount of samples in each bin normalized by maximum amount of samples in one bin.

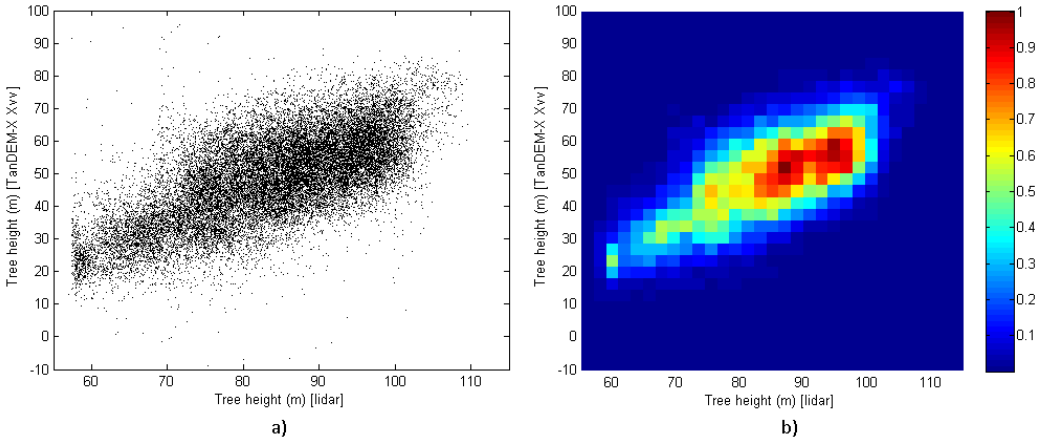

Figure 5.8: Relationship between TanDEM-X X-band interferometric height variations (m) using VV polarization (y-axis) and LIDAR height measurements (m) in forest areas (x-axis). a) Scatter plot representing this relationship. b) 2D histogram representing this relationship. Colors indicates the amount of samples in each bin normalized by maximum amount of samples in one bin.

	Correlation (%)	
	E-SAR	TanDEM-X
Ground	92,82%	78,75%
Forest	81,29%	61,77%

Table 5.1: Correlation between SAR height estimations and LIDAR height data for ground and forest areas.

has been made succesfully. On the other hand, TanDEM-X data provides not as good correlation as E-SAR due to the worse signal to noise ratio of the used images. However, the reasonably high correlation for open areas indicates that the interferometric processing for TanDEM-X images has been made correctly and the reflection location agreed with accurate ground elevation model. The correlation value gives also some estimate of phase center elevation overall accuracy for TanDEM-X interferometric images. In forested areas there is still significant correlation, but it is lower than for open areas. Partly this is caused by variable scattering center height in forest, but partly it can be explained also by the time difference between the measurements (trees have been grown higher in younger forests). These results show, that forest has clear effect on scattering center height in TanDEM-X images and therefore extraction of some tree height information from TanDEM-X images should be possible, especially when accurate ground model is available.

Chapter 6

Conclusions

In this work, recent X-band interferometric SAR data retrieved in the south of Finland by the satellites TerraSAR-X and TanDEM-X has been processed with the objective of obtaining canopy height information. In order to evaluate the precision of the results, they have been compared with forest height information obtained from X-band airborne E-SAR data acquired during the FINSAR campaign (52, 53, 54). Precise LIDAR measurements of the canopy height and terrain elevation over a test area have been used as reference.

Because there is no SAR processing toolbox widely available that supports the new TanDEM-X data format, the full preprocessing chain for this data was created. TanDEM-X COSAR files were transformed from *float16* complex samples to *float32* complex samples files by implementing a Java applet. The data was loaded into MATLAB and processed for generating the interferogram and the elevation map of the test area from two different SAR images. A preliminary comparison of the obtained elevation model with reference data was made. Airborne E-SAR X-band data was loaded into MATLAB and another elevation map of the same area has been also generated. All the data was geocoded to the WGS-84 UTM coordinate system and compared together. The whole chain of processing was validated by intercomparing the results with the reference and E-SAR data and checking that there was good agreement between them.

The final elevation maps obtained from the three different data sets presented good matching between each other, showing that TanDEM-X spaceborne SAR data can provide some estimate of the canopy height at forested areas. The obtained accuracy

was not nearly as good as that obtained with E-SAR airborne SAR data. Nevertheless, we consider that the lower precision of spaceborne SAR with respect to airborne SAR is compensated with its global coverage and its possibility of continuous monitoring. It should be kept in mind that this study provide early results based on one pair of spaceborne interferometric images. The analysis of a bigger amount of images can improve the results.

References

[1] Alliney, S. Spatial registration of multispectral and multitemporal digital imagery using fast-fourier transform techniques. *IEEE Transactions on Pattern Analysis and Machine Intelligence 15* (1993), 499–504. 37

[2] Axelsson, P. Processing of laser scanner data-algorithms and applications. *ISPRS J. Photogramm. Remote Sens. 33* (1998), 110–118. 49

[3] Brandfass, M., Hofmann, C., Mura, J., and Papathanassiou, K. Polarimetric sar interferometry as applied to fully polarimetric rain forest data. *Proc. IEEE Geosci. Remote Sens. Symp. 6*, 11 (July 2001), 2575–2577. 4

[4] Cutrona, L., Leith, E., Palermo, C., and Porcel, L. Optical data processing and filtering systems. *IRE Transactions on Information Theory IT-6* (1960), 386–400. 3

[5] Cutrona, L., Leith, E., Porcello, L., and Vivian, W. On the application of coherent optical processing techniques to synthetic-aperture radar. *Proceedings of the IEEE 51* (1966), 1026–1032. 3

[6] Cutrona, L., Vivian, W., Leith, E., and Hall, G. A high-resolution radar combat-surveillance system. *IRE Transactions on Military Electronics MIL-5* (1961), 127–131. 3

[7] Dammert, P., Lepparanta, M., and Askne, J. Sar interferometry over baltic sea ice. *Int. J. Remote Sens. 19* (1998), 3019–3037. 1

[8] Dastgir, N. Processing sar data using range doppler and chirp scaling algorithms, April 2007. 19, 41

[9] Elachi, C., and van Zyl, J. *Introduction to the Physics and Techniques of Remote Sensing.* Wiley, 2006. 6, 13, 23, 29, 34, 38

[10] European Space Agency (ESA). *ENVISAT Special Issue.* ESA Bulletin, no. 106, (June 2001). 4

[11] European Space Agency (ESA). *ERS-1 Spcecial Issue.* ESA Bulletin, no. 65, (June 1991). 4

[12] European Space Agency (ESA). *The ERS-2 Spacecraft and its Payload.* ESA Bulletin, no. 83, (August 1995). 4

[13] Fritz, T. Terrasar-x ground segment level 1b product format specification (10.12.2007). *ISPRS J. Photogramm. Remote Sens.* (2007). 48, 49, 60

[14] Gart, J. H. *Electronics and Aerospace Industry in Cold War Arizona, 1945-1968: Motorola, Hughes Aircraft, Goodyear Aircraft.* PhD. Arizona State University, 2006. 3

[15] German Aerospace Center (DLR). *TanDEM-X and TerraSAR-X in formation flight.* http://www.dlr.de/hr/desktopdefault.aspx/tabid-2317/3669_read-5488, accessed 23-March-2012. 46

[16] Geudtner, D., Vaehon, P., Mattar, K., and Gray, A. Radarsat repeat-pass sar interferometry. *Geoscience and Remote Sensing Symposium Proceedings, 1998. IGARSS '98 3* (1998), pp 1635–1637. 4

[17] Ghiglia, D., and Romero, L. Direct phase estimation from phase differences using fast elliptic partial differential equation solvers. *IEEE Transactions on Geoscience and Remote Sensing 15* (1989), 1107–1109. 41

[18] Goldstein, R., Barnett, T., and Zebke, H. Remote sensing of ocean currents. *Science 246* (1989), 1282–1285. 1

[19] Goldstein, R., Zebker, H., and Werner, C. Satellite radar interferometry: Two-dimensional phase unwrapping. *Radio Science 23* (1988), 713–720. 41

[20] Google Inc. *Satellite image.* Google Maps, 2012, https://maps.google.com/, accessed 03-May-2012. 45

[21] Graham, L. Synthetic interferometer radar for topographic mapping. *Proceedings of the IEEE 62* (1974), 763–768. 33

[22] Hajnsek, I., and Moreira, A. Tandem-x: Mission and science exploration. *Proc. Eur. Conf. Synthetic Aperture Radar (EUSAR)* (May 2006). 4

[23] Hajnsek, I., and Moreira, A. Tandem-x: Mission and science exploration. *Proc. Eur. Conf. Synthetic Aperture Radar (EUSAR), Dresden, Germany* (2006). 46

[24] Hanssen, R. Radar interferometry: Data interpretation and error analysis. *Dordrecht, The Netherlands: Kluwer Academic* (2001). 43

[25] Hanssen, R., and Bamler, R. Evaluation of interpolation kernels for sar interferometry. *IEEE Transactions on Geoscience and Remote Sensing 37* (1999), 318–321. 37

[26] Henderson, F., and Lewis, A. *Manual of Remote Sensing: Principles and Applications of Imaging Radar.* Wiley, 1998. 1, 6, 14, 18, 20, 25, 26

[27] Herland, E. A. Sar interferometry with ers-1 in forested areas. *Geoscience and Remote Sensing Symposium, 1995. IGARSS '95 1* (1995), 202–204. 4

[28] Kasischke, E. S., Christensen, N. L., and Bourgeau-Chavez, L. Relating forest biomass to sar data. *IEEE Trans. Geosci. Remote Sens. 33* (1995), 643–659. 4

[29] Kobayashi, S., Fujii, N., and Okubo, S. Detection of volcano deformations and coseismic movements using jers-1 l-band sar differential interferometry and combination with other geodetic measurements. *Geoscience and Remote Sensing Symposium, 1999. IGARSS '99 Proceedings. 2* (1999), 800–802. 4

[30] Krieger, G., Hajnsek, I.and Papathanassiou, K., Younis, M., and Moreira, A. Interferometric synthetic aperture radar (sar) missions employing formation flying. *Proceedings of the IEEE 98*, 5 (2010), 816–843. 47, 48

[31] Kwoh, L., Chang, E., Heng, W., and Hock, L. Dtm generation from 35-day repeat pass ers-1 interferometry. *Geoscience and Remote Sensing Symposium 1994. IGARSS '94 4* (1994), 2288–2290. 4, 37

[32] Lame, D. B., and Born, G. H. Seasat measurement system evaluation: Achievement and limitations. *Journal Of Geophysical Research 87*, C5 (1982), 3175–3178. 3

[33] Le Toan, T., Beaudoin, A., Riom, J., and Guyon, D. Relating forest biomass to sar data. *IEEE Trans. Geosci. Remote Sens. 30* (1992), 403–411. 4

[34] Li, F., and Goldstein, R. Studies of multibaseline spaceborne interferometric synthetic aperture radars. *IEEE Transactions on Geoscience and Remote Sensing 28* (1990), 88–97. 42

[35] Li, F., and Raney, R. Prolog to special section on spaceborne radars for earth planetary observations. *Proceedings of the IEEE 79* (1991), 776–776. 4

[36] Liao, M., Lin, H., and Zhang, Z. Automatic registration of insar data based on least-square matching and multistep strategy. *Photogrammetric Engineering & Remote Sensing 70*, 10 (2004). 37

[37] Lin, Q., Vesecky, J., and Zebker, H. New approaches in interferometric sar data processing. *IEEE Transactions on Geoscience and Remote Sensing 30* (1992), 560–567. 37

[38] Lin, Y., and Sarabandi, K. A monte carlo coherent scattering model for forest canopies using fractal-generated trees. *IEEE Trans. Geosci. Remote Sens. 37*, 1 (1999), 440–451. 4

[39] Lin, Y., and Sarabandi, K. Retrieval of forest parameters using a fractal based coherent scattering model and a genetic algorithm. *IEEE Trans. Geosci. Remote Sens. 37*, 3 (1999), 1415–1424. 4

[40] Liu, D., Sun, G., Guo, Z., Ranson, K., and Du, Y. Three-dimensional coherent radar backscatter model and simulations of scattering phase center of forest canopies. *IEEE Trans. Geosci. Remote Sens. 48*, 1 (2010), 349–357. 4

[41] Love, A. W. In memory of carl a. wiley. *IEEE Antennas and Propagation Society Newsletter* (June 1985), 17–18. 3

[42] Madsen, S., Zebker, H., and Martin, J. Topographic mapping using radar intereferometry: processing techniques. *IEEE Transactions on Geoscience and Remote Sensing 31* (1993), 246–256. 42

[43] Massonnet, D., Briole, P., and Arnaud, A. Deflation of mount etna monitored by spaceborne radar interferometry. *Nature 375* (1995), 567–570. 1

[44] Massonnet, D., Rossi, M., Carmona, C., Adragna, F., Peltzer, K. F., and T. Rabaute, G. The displacement field of the landers earthquake mapped by radar interferometry. *Nature 364* (1993), 138–142. 1

[45] Mette, T., Papathanassiou, K., and Hajnsek, I. Biomass estimation form polarimetric sar interferometry over heterogenous forest terrain. *Proc. IGARSS04, Anchorage 1* (2004), 511–514. ii, 1

[46] Nemoto, Y., Nishino, H., Ono, M., Mizutamari, H., Nishikawa, K., and Tanaka, K. Japanese earth resources satellite-1 sythetic aperture radar. *Proceedings of the IEEE 79* (1991), 800–809. 4

[47] Oppenheim, A., and Lim, J. The importance of phase in signals. *IEEE Trans. Comput. 69* (1981), 529–541. 37

[48] Palacios, R. Function to convert lat./lon. vectors into utm coordinates. Matlab Central, 2006, http://www.mathworks.com/matlabcentral/fileexchange/10915, accessed 18-April-2012. 59

[49] Papathanassiou, K., and S. R. Cloude, S. Single-baseline polarimetric sar interferometry. *IEEE Trans. Geosci. Remote Sens. 39*, 11 (2001), 2352–2363. 4

[50] Papathanassiou, K., and S. R. Cloude, S. Three-stage inversion process for polarimetric sar interferometry. *Proc. Inst. Elect. Eng.-Radar Sonar Navig. 150*, 3 (2003), 125–134. 4

[51] PCI Geomatics. *Geometric Distortions.* , http://www.pcigeomatics.com/images/Geometric_Distortions.jpg, accessed 21-February-2012. 27

[52] Praks, J., Antropov, O., and Hallikainen, M. Lidar-aided sar interferometry studies in boreal forest: Scattering phase center and extinction coefficient at x- and l-band. *IEEE Trans. Geosci. Remote Sens. PP*, 99, 1–13. ii, 2, 4, 5, 67, 69, 73

[53] Praks, J., Hallikainen, M., and Yu, X. Studies of phase center and extinction coefficient of boreal forest using x- and l-band polarimetric interferometry combined with lidar measurements. *Proc. POLINSAR 668* (2009), 466–470. ii, 2, 4, 5, 73

[54] Praks, J., Kugler, F., Papathanassiou, K., Hajnsek, I., and Hallikainen, M. Height estimation of boreal forest: Interferometric model-based inversion at l- and x-band versus hutscat profiling scatterometer. *IEEE Trans. Geosci. Remote Sens. 4*, 3 (2007), 466–470. ii, 2, 4, 5, 73

[55] Pulliainen, J. T., Kurvonen, L., and Hallikainen, M. Relating forest biomass to sar data. *IEEE Trans. Geosci. Remote Sens. 37* (1999), 927–937. 4

[56] Raney, R. K., Luscombe, A. P., Langham, E. J., and Ahme, A. Radarsat. *Proc. IEEE* (February 1991). 4

[57] Rodriguez, E., and Martin, J. Theory and design of interferometric synthetic aperture radars. *Proc. Inst. Elect. Eng. F, Radar Signal Process 139* (1992), 147–159. 42

[58] Roth, A., Huber, M., and Kosmann, D. Geocoding of terrasar-x data. *Proc. of 20th International Congress of the ISPRS, Istanbul, Turkey, Commission III* (2004), 840–844. 30

[59] Rufino, G., Moccia, A., and Esposito, S. Dem generation by means of ers tandem data. *IEEE Transactions on Geoscience and Remote Sensing 36* (1998), 1905–1922. 37

[60] Saunders, R., and Pettengi, G. Magellan: Mission summary. *Science 252* (1991), 247–249. 3

[61] Scheiber, R., and Moreira, A. Coregistration of interferometric sar images using spectral diversity. *IEEE Transactions on Geoscience and Remote Sensing 38* (2000), 2179–2191. 37

[62] Sherwin, C. W., Ruina, J. P., and Rawcliffe, R. D. Some early developments in synthetic aperture radar systems. *IRE Transactions on Military Electronics* (April 1962), 111–115. 3

[63] Shurong, P., et al. A high accurate approach for insar flat earth effect removal. *Measuring Technology and Mechatronics Automation, 2009. ICMTMA '09. International Conference on 3* (2009), 742–745. 57

[64] Stangl, M., et al. Terrasar-x technologies and first results. *Proc. Inst. Elect. Eng. Radar, Sonar Navig. 153* (2006), 86–95. 46

[65] Sun, G., and Ranson, K. Three-dimensional radar backscatter model of forest canopies. *IEEE Trans. Geosci. Remote Sens. 33*, 2 (1995), 372–382. 4

[66] Thirion, L., Colin, E., and Dahon, C. Capabilities of a forest coherent scattering model applied to radiometry, interferometry, and polarimetry at p- and l-band. *IEEE Trans. Geosci. Remote Sens. 44*, 4 (2006), 849–861. 4

[67] Tomiyasu, K. Tutorial review of synthetic aperture radar with application to imaging of the ocean surface. *Proceedings of the IEEE 66* (1978), 563–583. 19

[68] Treuhaft, R., et al. Vegetation characteristics and underlying topography from interferometric radar. *Radio Sci. 31*, 6 (1996). 4

[69] Treuhaft, R., et al. Vegetation profiles in tropical forests from multibaseline interferometric synthetic aperture radar, field, and lidar measurements. *J. Geophys. Res. 114*, D23 (2009). 4

[70] Treuhaft, R., Law, B., Asner, G., and Hensley, S. Vegetation profile estimates from multialtitude, multifrequency radar interferometric and polarimetric data. *IEEE Trans. Geosci. Remote Sens. 1* (2000), 126–128. 4

[71] Treuhaft, R., and Siqueira, P. The vertical structure of vegetated land surfaces from interferometric and polarimetric radar. *Radio Sci. 35*, 1 (2000). 4

[72] Wauthier, C., et al. L-band and c-band insar studies of african volcanic areas. *Geoscience and Remote Sensing Symposium,2009 IEEE International,IGARSS 2009 2* (2009), II–210–II–213. 4

[73] Werninghaus, R., and Buckreuss, S. The terrasar-x mission and system design. *IEEE Trans. Geosci. Remote Sens. 48* (2010), 606–614. 4

[74] Wikipedia Contributors. *Diagram of circular polarisation*, Wikimedia Foundation Inc. Wikipedia the free encyclopedia, 2007, http://commons.wikimedia.org/wiki/File:Polarisation_(Circular).svg, accessed 20-March-2012. 9

[75] Wikipedia Contributors. *Diagram of elliptical polarisation*, Wikimedia Foundation Inc. Wikipedia the free encyclopedia, 2007, http://en.wikipedia.org/wiki/File:Polarisation_(Elliptical).svg, accessed 20-March-2012. 9

[76] Wikipedia Contributors. *Diagram of linear polarisation*, Wikimedia Foundation Inc. Wikipedia the free encyclopedia, 2007, http://commons.wikimedia.org/wiki/File:Polarisation_(Linear).svg, accessed 20-March-2012. 9

[77] Wikipedia Contributors. *Electromagnetic opacity of the Earth's atmosphere*, Wikimedia Foundation Inc. Wikipedia the free encyclopedia, 2008, http://en.wikipedia.org/wiki/File:Atmospheric_electromagnetic_opacity.svg, accessed 22-March-2012. 15

[78] Wikipedia Contributors. *Ona electromagnètica*, Wikimedia Foundation Inc. Wikipedia the free encyclopedia, 2007, http://ca.wikipedia.org/wiki/Fitxer:Onde_électromagnétique_ca.png, accessed 20-March-2012. 7

[79] Wiley, C. A. Synthetic aperture radars: A paradigm for technology evolution. *IEEE Transactions on Aerospace and Electronic Systems*, 3 (May 1985), 440–443. 3

[80] Williams, M. The theory for a forward sar model: Implementation, applications and challenges. *Proc. EUSAR* (May 2006). 4

[81] Zebker, H., and Villasenor, J. Decorrelation in interferometric radar echoes. *IEEE Transactions on Geoscience and Remote Sensing 30* (1992), 950–959. 42, 43

[82] Zianis, D., Muukkonen, P., Mäkipää, R., and Manuccini, M. Biomass and stem volume equations for tree species in europe. *Silva Fennica Monographs 4* (2005), 1–63. ii, 1